THE ASTROPHYSICAL JOURNAL, 476:403–427, 1997 February 10
© 1997. The American Astronomical Society. All rights reserved. Printed in U.S.A.

THE HELIUM VALLEY: COMPARISON OF IMPULSIVE SOLAR FLARE ION ABUNDANCES AND GYRORESONANT ACCELERATION WITH OBLIQUE TURBULENCE IN A HOT MULTI-ION PLASMA

JÜRGEN STEINACKER
Max-Planck-Gesellschaft, Arbeitsgruppe "Staub in Sternentstehungsgebieten," Schillergäßchen 2-3, 07745 Jena, Germany; stein@astro.uni-jena.de

JEAN-PAUL MEYER
Service d'Astrophysique, CEA/DSM/DAPNIA, Centre d'Etudes de Saclay, 91191 Gif-sur-Yvette, France; meyer@sapvxb.saclay.cea.fr

ADRIANE STEINACKER
Max-Planck-Gesellschaft, Arbeitsgruppe "Staub in Sternentstehungsgebieten," Schillergäßchen 2-3, 07745 Jena, Germany; adriane@astro.uni-jena.de

AND

DONALD V. REAMES
Laboratory for High Energy Astrophysics, Code 661, NASA/Goddard Space Flight Center, Greenbelt, MD 20771; reames@lheavx.gsfc.nasa.gov
Received 1995 July 24; accepted 1996 July 25

ABSTRACT

We present a detailed interpretation of the heavy ion abundance enhancements observed in impulsive flare energetic particles, in terms of the conditions for gyroresonant acceleration by moderately oblique waves in a hot solar coronal plasma.

On the basis of a realistic coronal plasma containing its complete set of minor ions, we analyze first all parallel wave modes in terms of their dispersion relation, damping timescale, and condition for gyroresonant acceleration of thermal ions, as a function of temperature. We identify the "Helium Valley," the region in the frequency-wavenumber plane of strong wave damping by thermal $^4He^{+2}$ ions, as crucial for explaining the observed abundances: any ions with charge-to-mass ratio in the neighborhood of 0.5 cannot be accelerated preferentially, relative to $^4He^{+2}$.

Then solving the dispersion relation equation for oblique waves in a hot *e*-*p*-He plasma, we discuss this general class of waves in terms of polarization and damping timescale. For waves propagating at moderate angles to the magnetic field ($\theta \gtrsim 90°$), our calculations indicate that the first harmonic $n = 1$ gyroresonance is dominant, and that the corresponding He valley narrows down for increasing angle θ. Using this analysis, we calculate the limits of the He valley and investigate the preferential gyroresonant acceleration of heavy ions by moderately oblique waves ($\theta \gtrsim 90°$) in a solar coronal plasma. Only for nearly perpendicular waves ($\theta \approx 90°$), are higher order resonances important and regions of wave damping by interaction with thermal particles vanishingly narrow in frequency.

We estimate the fraction of ions of each element outside the He valley as a function of temperature and compare the resulting enhanced abundances with the observed enhancements, for the case of a spectrum of non–quasi-perpendicular waves, as produced by a cascading of the general turbulence. The results allow us to specify the range of possible temperatures for the source plasma of the accelerated particles to between ~ 2.4 and $\sim 4.5 \times 10^6$ K, i.e., comparable to active region (AR), but not to flaring gas, temperatures. This points to an acceleration of the ions taking place, either in the AR gas surrounding the flare itself or within the flaring loop but before it became heated. Constraints are set on the typical time Δt over which the ions are accelerated preferentially. We find times between $\sim 5 \times 10^{-4}$ and $\sim 3 \times 10^{-2}$ s (for our nominal plasma with density and field of $n_e = 10^{10}$ cm^{-3} and $B = 100$ G); it could be ~ 10 times larger, if the typical conditions in quiescent ARs ($n_e \sim 2 \times 10^9$ cm^{-3} and $B \sim 200$ G) apply also to the bulk $\sim 3 \times 10^6$ K gas of flaring ARs. We discuss another physical interpretation of Δt, if wave cascading is effective. Preliminary calculations have shown that the proposed selective acceleration mechanism can be applied in underdense ($\omega_p/\Omega_e < 1$) as well as in overdense plasmas (our nominal case), provided that quasi-perpendicular waves (generated, e.g., by an electron beam) are not dominant.

Subject headings: acceleration of particles — plasmas — Sun: abundances — Sun: corona — Sun: flares — Sun: magnetic fields — Sun: particle emission

1. INTRODUCTION

In recent years, a special type of solar flare, denoted "impulsive" after the duration of the event-related soft X-ray emission, has attracted the interest of both observers and theoreticians. These flares are located at coronal heights $< 10^5$ km (Pallavicini, Serio, & Vaiana 1977) and are rarely associated with type II radio emission, indicating coronal shock structures (Cane, McGuire, & von Rosenvinge 1986).

It has been known for some time that impulsive flare energetic particles often show a huge enhancement of the ^{3}He isotope, and more modest enhancements of some heavy elements, relative to coronal abundances (e.g., Reames 1990). This heavy element composition has been examined

recently in detail by Reames, Meyer, & von Rosenvinge (1994, hereafter RMvR), based on data from the *ISEE 3* spacecraft for a large sample of impulsive events (see also Reames 1993, 1995). Their results can be summarized as follows:

1. The accelerated ions have been extracted out of a gas with typical "coronal" composition. This composition differs from that of the photosphere by an excess of those elements with first ionization potential (FIP) $\lesssim 10$ eV relative to heavy elements with higher FIP (and probably to H; e.g., Meyer 1985b, 1993a, 1993b, 1996a, 1996b).

2. Besides the frequently observed huge enhancements of ^{3}He/^{4}He by factors of up to $\sim 20{,}000$ (observable only when the enhancement exceeds a factor of ~ 200), the accelerated particles show on the average no enhancement of ^{4}He, C, N, and O relative to each other, mean enhancements of Ne, Mg, and Si by roughly equal factors of ~ 2.6 relative to CNO, and a mean enhancement of Fe by factors of ~ 7.5 and ~ 2.8 relative to CNO and to NeMgSi, respectively. Studies by Mason et al. (1986) and Mason, Mazur, & Hamilton (1994), however, suggest that O is sometimes moderately enhanced relative to C. However, the more comprehensive investigation of RMvR shows that this is definitely not the more common situation.

3. The variability of these enhancements is surprisingly limited: factors of ~ 2.6, ~ 2, and ~ 1.5 around the mean value for Fe/CNO, NeMgSi/CNO, and Fe/NeMgSi, respectively, and factors of $\lesssim 1.5$ for Ne/Mg, Ne/Si, and Mg/Si (all at the 95% probability level).

4. These observational results have been analyzed with plain consistency arguments, based on the simple hypothesis that ions with the same charge to mass ratio Q/A cannot be preferentially accelerated relative to one another by plasma waves. Note that ^{4}He and ^{12}C are fully stripped, with $Q/A = 0.5$, at all relevant gas temperatures. Hereafter, "preferential acceleration" will denote preferential acceleration relative to ^{4}He and C (C is essentially ^{12}C). It was shown that the observed composition implies that the ions have been selected for preferential acceleration in a gas with temperature around $\sim 3.5 \times 10^6$ K (between ~ 2.5 and $\sim 5 \times 10^6$ K), a result that will be confirmed and refined in the present analysis. At higher temperatures, indeed, ^{20}Ne rapidly becomes fully stripped ($Q/A = 0.5$), while ^{28}Si still retains one or two orbital electrons, making it difficult to understand the very similar and stable enhancements of Ne and Si. At lower temperatures, ^{16}O starts to retain one or two orbital electrons and have Q/A values similar to those of Ne, Mg, and Si ions, making it difficult to understand the lack of enhancement of O relative to C. The associated requirement that no significant fraction of the source material lies below 2.5×10^6 K is actually quite strict.

5. As for ^{56}Fe, its Q/A is ~ 0.28 around $\sim 3.5 \times 10^6$ K, as compared to $Q/A \sim 0.42$ for the predominant Ne, Mg, and Si ions. Fe may therefore be accelerated out of the same $\sim 3.5 \times 10^6$ K gas as Ne, Mg, and Si, its larger enhancement being simply due to a more efficient acceleration of lower Q/A ions. An additional acceleration of Fe out of hotter gases up to $\sim 10 \times 10^6$ K is in principle possible, and it cannot a priori be excluded if the acceleration of Ne, Mg, and Si out of such hotter gases turns out to be prevented entirely by their ionization states at high temperature.

6. Very high charge states have been observed by Luhn et al. (1987) for the energetic Fe ions, corresponding to equilibrium temperatures largely beyond $\sim 10 \times 10^6$ K. This measurement needs confirmation. First, it conflicts with the earlier one by Ma Sung et al. (1981). Second, similar measurements performed by the same instrument on *gradual* event Fe charge states (Luhn et al. 1985) disagree by about four charge units with other measurements at comparable ~ 1 MeV nucleon^{-1} energies (Gloeckler et al. 1976; Mason et al. 1995), although they do agree with higher energy ones in the 15–600 MeV nucleon^{-1} range (Tylka et al. 1995; Leske et al. 1995). So there exists a hint that Luhn et al. (1987)'s charge scale for Fe might possibly be systematically shifted. Note that Luhn et al. (1987) also found Si fully stripped, though with a very poor charge resolution. If Luhn et al. (1987)'s measurements are confirmed, a stripping after the ion removal from the thermal pool, possibly by energetic electrons, seems required to account for the high charge states.

This temperature of $\sim 3.5 \times 10^6$ K obtained for the source gas of the escaping accelerated particles is comparable to that of the ordinary active region (AR) gas preexisting and surrounding the much hotter, flaring gas itself (see Appendix A). The strict condition that little source gas lies below $\sim 2.5 \times 10^6$ K might be understood in terms of the shape of the radiative loss function (see Appendix A). Note that the broad γ-ray line study by Murphy et al. (1991) suggests that the composition of the trapped accelerated particles is, by and large, similar to that of the escaping ones.

From the theoretical point of view, the impulsive flare environment is a natural one to study particle acceleration in electric fields produced by reconnection or by interaction with plasma turbulence, since, in the highly magnetized plasma, perturbations are expected to propagate mainly with the Alfvén speed, so that the formation of strong shocks is unlikely. As far as electric field acceleration of thermal plasma is concerned, direct acceleration in double layers leads to a continuous energization of all ions. Special and somewhat artificial assumptions are necessary to accelerate some of the ions preferentially (Winglee 1989, using multistream instability).

Therefore, different models, based on gyroresonant interaction with plasma waves, have been proposed to overcome the problem of the puzzling overabundances, especially of the ^{3}He isotope (Ibragimov & Kocharov 1977; Fisk 1978; Kocharov & Kocharov 1984; Hayakawa 1983; Varvoglis & Papadopoulos 1983; Weatherall 1984; Schlickeiser & Steinacker 1989; Riyopoulos 1991; Ohsawa 1993; Zhang 1995). This approach is attractive, since the complex conditions for gyroresonant interaction between plasma waves and ions guarantee a sufficient number of selection mechanisms. Now, in any such model dealing with overabundances of energetic particles in impulsive solar events, two types of ingredients play a crucial role.

First, the assumed properties of the source plasma of the escaping energetic particles have to be specified. For this source plasma, one might at first have considered the hot flaring gas itself. However, the results of RMvR discussed above indicate that the escaping particles originate in the cooler $\sim 3.5 \times 10^6$ K plasma of the AR in which the flare develops, rather than in this hot gas itself.

Due to the dominant abundances of protons and ^{4}He^{+2}, it is in most cases sufficient to treat the plasma as an *e-p-*^{4}He^{+2} plasma, and to consider other ions in a test particle

approach. Then, for all species considered, the density has to be specified. The relative densities of the various elements are known fairly accurately for the coronal background plasma (Appendix B). But the absolute density in AR plasmas is more variable, lying typically in the range from ~ 1 to $\sim 4 \times 10^9$ cm^{-3}, with magnetic fields on the order of ~ 50 to ~ 400 G (Appendix A). These values refer mainly to quiescent ARs, but, according to the scarce indications we have, it does not seem that the bulk $\sim 3 \times 10^6$ K gas of those ARs in which a flare takes place is very different; however, caution on this point is required. With the above values, the plasma frequency to electron gyrofrequency ratio $\omega_p/\Omega_e = 3.2 \times 10^{-3}(n_e)^{1/2}/B$ lies between ~ 0.25 and ~ 4, so that the plasma typically lies on either side in the neighborhood of the underdense-overdense limit $\omega_p/\Omega_e = 1$ (Appendix A). Thus, it seems plausible that the source plasma is sometimes slightly overdense (as was often assumed; e.g., Miller & Steinacker 1992, where $n_e = 10^{10}$ cm^{-3} and $B = 100$ G), and sometimes slightly underdense (as assumed by Miller & Viñas 1993, where $n_e = 10^{10}$ cm^{-3} and $B = 1000$ G, thus allowing wave generation by electron beams). Note, however, that, given the time-dependent, complex structure of the magnetic field, only mean values of the field and density in the AR plasma can be assessed. Further, almost all models assume that the field is locally homogeneous.

To study the general features of the wave modes allowed in the assumed plasma, temperature effects may be neglected, so that the cold plasma approximation can be applied. Detailed investigations of wave-damping effects, however, require the consideration of the temperature of each particle species, or even of different populations of the same species. Miller & Viñas (1993) consider a plasma at a temperature of 10^6 K, which is too low, hit by a hot 10^7 K electron population drifting with an energy of 5 keV. In Miller, Viñas, & Reames (1993b), a more realistic temperature of 3×10^6 K is used for the ambient plasma, but with an energy of the drifting electrons of 10 keV.

Second, the origin and the type of the waves have to be specified. Numerous instabilities have been proposed to produce plasma modes of various kinds (e.g., electrostatic ion cyclotron waves by Fisk 1978; electrostatic two-ion hybrid waves by Riyopoulos 1991; and electromagnetic ion cyclotron waves by Temerin & Roth 1992). These models were designed primarily to explain the huge enhancement of $^3He^{+2}$ by injecting a large amount of wave energy close to the gyrofrequency of this rare ion, some of them dealing with the much more moderate heavy-element enhancements, as well.

A promising suggestion for an efficient wave generation mechanism is beam instability, in which a hot population of particles drifts through the flare plasma. Temerin & Roth (1992) have recently considered ^{3}He acceleration by waves generated by energetic electron beams, thus accounting for the observed association between ^{3}He enrichments, high electron intensities, and type III bursts; contrary to earlier ones, this scenario also does not require a high ^{4}He/p ratio in the gas, which indeed is not observed (RMvR). On this basis, Miller & Vinãs (1993) and Miller, Vinãs, & Reames (1993a, 1993b) (hereafter MV, MVRa, and MVRb, respectively) have explored a more complete model with a detailed investigation of the wave generation, and a wave-particle simulation to study the ion acceleration process. They considered a nonrelativistic electron beam drifting along the magnetic field and producing quasi-perpendicular proton cyclotron and shear Alfvén waves, R waves, and electrostatic waves, which interact with ions in the first harmonic of their gyrofrequency. Such a wave generation mechanism may also explain Luhn et al. (1987)'s observed high charge states in terms of a late ionization by the beam electrons. But the wave generation can take place only in an underdense plasma, with $\omega_p/\Omega_e < 1$. In addition, the role of higher orders of gyroresonance, which become crucial for very obliquely propagating waves, remains to be investigated.

Recently, Zhang (1995) has provided a new development of Fisk (1978)'s approach in terms of electrostatic ion cyclotron waves, removing the earlier requirement of a high ^{4}He/p ratio in this type of model. Since the required electrostatic waves are also generated by electron beams, this model, like MV's, accounts for the association between ^{3}He enrichments, high electron fluxes, and type III bursts, as well as for the late stripping of the accelerated ions (for which the author, however, considers another alternative: the late heating of the flaring plasma, applicable in *extremely* impulsive flares only). Direct acceleration to the observed MeV energies is not possible, so that a two-step acceleration process is required.

In another approach, the turbulence near the flare site can be inferred from the wave spectra measured in the interplanetary space during impulsive flare events. Such spectra extend over a broad range of wavenumbers, probably due to wave cascading from turbulence injected by large-scale fluctuations on the solar surface, and they cover all propagation angles θ (see, e.g., Tu, Marsch, & Thieme 1989; Zhou & Matthaeus 1990; Miller & Roberts 1995). In this picture, the originally injected energy is distributed over all wavenumbers, and extreme preferential acceleration, as observed for ^{3}He, is hard to achieve. It is this general turbulence scenario for heavy ion acceleration that we want to treat in this paper, by expanding former studies to a more general analysis of wave-particle interaction in the warm AR plasma in which an impulsive flare develops. We will interpret the selective acceleration of specific heavy elements in terms of the damping of waves by interaction with the ions, and particularly with the abundant $^4He^{+2}$ ions. For this first illustration of the possible effects of wave damping on the accelerated particle composition, we will not treat wave generation and cascading and wave-particle interaction simultaneously: we will simply investigate the effect of damping on an initially smooth wave spectrum and assume that the wave energy is deposited instantaneously; this latter simplifying assumption will be discussed in § 4.2. Of course, such a mechanism can work only if the injected energy of the waves is not so large that their damping is insignificant, even when all $^4He^{+2}$ ions in the gas have been accelerated. Further, it can be effective only when the predominant waves in the plasma are not quasi-perpendicular. No limitations are required on the ^{4}He/p ratio. Since the conditions for wave damping depend on n_e and B, we have performed preliminary calculations indicating that the selective acceleration process basically works equally well for overdense and underdense plasmas.

We start our analysis in § 2 by illustrating the frequency range of wave damping by thermal ions for the case of parallel waves in a multicomponent plasma with realistic coronal composition. Calculating the hot plasma dispersion relation, we assess the frequency ranges of wave damping by

the various heavy ions, and in particular the crucial "helium valley" due to heavy damping by $^4He^{+2}$. We estimate the damping timescales for any kind of parallel turbulence and present the time evolution of any injected parallel turbulence in the flare associated plasmas. In § 3, we generalize our treatment to oblique propagating waves, but in a simpler hot electron-proton-helium plasma, in view of the dominant role of wave damping by $^4He^{+2}$. Thus, we investigate the influence of the propagation angle on the limits of the dominant He valley. Under the assumption that the waves are not predominantly propagating nearly perpendicular to the magnetic field, we derive in § 4 the fraction of ions outside the He valley, where they can be accelerated preferentially. Comparison with the observed abundance enhancements enables us to specify better the temperature limits for the source gas out of which the ions have been accelerated, and to determine the timescales over which *either* ions are accelerated preferentially *or* the effect of wave cascading becomes important. In § 5, we summarize our results. Appendix A discusses the temperature, density, and magnetic field in AR source plasmas. Appendix B gives a brief summary of the updated ion abundances being used throughout the paper for this coronal source gas. In Appendix C, the complicated behavior of the wave polarization in a cold *e-p*-He plasma is described, which is essential for the interpretation of our results on oblique propagating waves in § 4.

2. PARALLEL PLASMA WAVES IN THE REALISTIC HOT MULTI-ION SOLAR CORONAL PLASMA

The basic idea of gyroresonant interaction between particles and waves is that particles will interact with waves that have a frequency close to their gyrofrequency or its harmonics. Therefore, a complete analysis of ion acceleration requires a detailed knowledge of the possible wave modes around all relevant gyrofrequencies. This can be done only in a multi-ion plasma approach.

The best way to describe plasma waves is to find their dispersion relation $\omega(\boldsymbol{k})$, which relates the frequency ω to the wavevector $\boldsymbol{k}$. For convenience, we will often use normalized quantities ω/Ω_p and $|\boldsymbol{k}|c/\Omega_p$, where Ω_p is the proton gyrofrequency. The dispersion relation $\omega(\boldsymbol{k})$ can be calculated in different approaches. The simplest approximation is the cold plasma approximation, neglecting the thermal velocity distribution of the background particles. Because our interest is focused on determining not only which waves are possible in the multi-ion plasma, but also which waves are actually available to accelerate ions, we have to go one step further and allow the background particles to form a thermal distribution, in order to account for thermal damping effects. This more complicated so-called hot plasma dispersion relation contains a complex frequency $\omega_c = \omega - i\omega_{\rm im}$. The real part of ω_c is the plain frequency, denoted simply by ω. The amplitudes of the waves are now $\propto|\exp(-i\omega_c t)| \propto \exp(-\omega_{\rm im} t)$ and describe damping or growth, depending on the sign of $\omega_{\rm im}$.

Both approaches are reviewed in detail for an electron-proton plasma and parallel waves in Steinacker & Miller (1992, hereafter SM) and Miller & Steinacker (1992). In the following, we will start our treatment with the simple case of parallel waves [$\boldsymbol{k} \equiv (0, 0, k)^t$], because of their importance, and in order to keep the number of generalizations at an appropriate level. The case of waves propagating at an angle to the magnetic field will be discussed in § 3.

2.1. *Range of Damping by Thermal Ions*

To see which wave types are important, it is helpful to study the parallel waves in a cold electron-proton-helium plasma (for details, see SM and Appendix C). Figure 1 shows the dispersion relation $\omega(k)$ for this case, for the nominal magnetic field of $B = 100$ G and electron density of $n_e = 10^{10}$ cm^{-3} used throughout this paper. In the low-frequency region, both the right-hand polarized waves (R waves, *dashed line*) and the left-hand polarized waves (L waves, *solid lines*) follow the linear Alfvén dispersion relation. Near the helium gyrofrequency $\omega/\Omega_p = 0.5$, the L waves resonate with the left-gyrating $^4He^{+2}$ ions, and the dispersion relation of the L waves bends over to the helium cyclotron wave region. After a gap in frequency, in which waves cannot propagate in the plasma, L waves start to exist above the cutoff frequency $\omega/\Omega_p \sim 0.57$ with a high phase speed. For low k, these waves first have a much higher phase speed ω/k than the previous ones, and then they head toward the proton cyclotron wave region at $\omega/\Omega_p \lesssim 1$. The R waves are unaffected by helium ions and protons, reach above $\omega/\Omega_p = 1$ the Whistler region where $\omega \propto k^2$, and have a resonance with the right-gyrating electrons at $\omega/\Omega_p = m_p/m_c = 1836$, far beyond the upper limit of Figure 1 at $\omega/\Omega_p = 1$.

A qualitative way to investigate the influence of thermal particles on the waves without calculating the complicated hot plasma dispersion relation is to calculate the range of waves that are able to gyroresonate with thermal particles. Therefore, we consider the gyroresonance condition

$$\omega = kv\mu + \frac{n\Omega}{\gamma}, \tag{1}$$

for interaction of a particle with charge q, mass m, velocity v, pitch angle cosine μ, nonrelativistic gyrofrequency $\Omega = qB/mc$, and Lorentz factor γ, with a parallel L (R) wave of order $n = +1$ (-1). Directly relevant to the wave-particle resonance is the particle velocity component along the field direction $v_z = v\mu$. Equation (1) can be interpreted as a straight line in the (ω-k) plane. The intersections of this line with the dispersion relation define the waves (k, ω) that can interact with the particle (detailed examples for this technique are shown in SM). In the following, we will restrict our considerations to ion–L wave interactions, i.e., to $n = +1$, because thermal ions and R waves can interact only at very high k values, deep in the electron cyclotron region at very high frequencies, where the electrons damp all available waves (see SM).

For a thermal ion of species i with a nonrelativistic speed close to the most probable thermal speed $v_i = (2kT/m_i)^{1/2}$ ($\gamma_i \sim 1$) and a gyrofrequency Ω_i, all lines describing the gyroresonance condition (1) in the (ω-k) plane therefore start at the point $(0, \Omega_i)$ and have the slope $v_z = v\mu$. For an assumed Maxwell distribution, the bulk of the ions have a velocity $v < \eta v_i$, where $\eta \sim 1$ or a few units. For an isotropic distribution in pitch angle $(-1 \leq \mu \leq \pm 1)$, the range in the (ω-k) plane, in which most thermal ions of species i are able to interact with waves, can thus be represented very roughly by the limiting lines $\omega = \pm k\eta v_i + \Omega_i$.

But here we are interested in wave damping, and we want to define a different region in the (ω-k) plane, the "damping range" over which waves are effectively damped by interaction with ions of species i. This range, obviously, depends on the ion abundance. Figure 2 gives a comparative view of

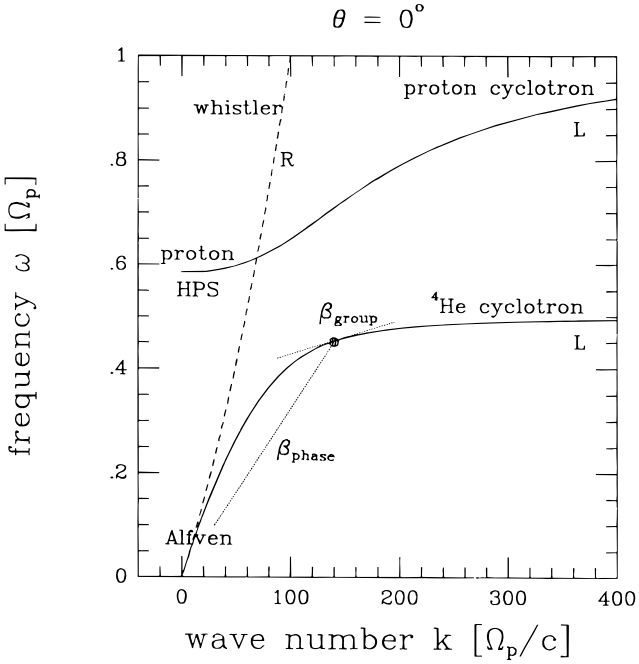

FIG. 1.—Cold plasma dispersion relation $\omega(k)$ of parallel waves ($\theta = 0°$) for a plasma with $B = 100$ G and $n_e = 10^{10}$ cm^{-3}. The different wave types are indicated, as well as the sense of polarization (R for right-handed and L for left-handed). In addition, the normalized phase speed $\beta_{\rm phase} = \omega/kc$ is illustrated as the slope of the line connecting the point (k_0, ω_0) to the origin, and the normalized group speed $\beta_{\rm group} = \partial\omega/\partial kc|_{k_0}$ is shown as the slope of the tangential line at this point. "HPS" stands for "high phase speed" waves.

the Maxwell distributions, for the most important ions in a $T = 4 \times 10^6$ K coronal plasma (Appendix B). For each ion species i, it is convenient to define some limiting value of $|v_z|$, $v_{{\rm lim},i}$ up to which the contribution of ions i to the damping of waves is considered significant. Choosing the same limiting speed $v_{{\rm lim},i}$ for all ion species i would not be an appropriate choice, since, obviously, there are many more protons than, e.g., $^{16}O^{+8}$ or $^3He^{+2}$ ions beyond any such fixed $v_{{\rm lim},i}$. The same would apply if $v_{{\rm lim},i}$ were chosen as a fixed multiple of the ion's thermal speed v_i. To estimate roughly the ranges of effective wave damping by the various ions with widely different densities, we therefore consider, for each particular ion, the range of speeds v_z over which its differential density lies above a fixed value $[dn_i/dv_z]_{\rm lim} = 10^{-6} \times dn_p/dv_z|_{v_z=0}$ in terms of the proton differential density at $v_z = 0$. This limit, resulting in a limiting value of $v_{{\rm lim},i}$ for each particular ion i, has been chosen so as to yield a finite damping region for all ions with abundance down to that of the rare isotope $^3He^{+2}$. In this way, we have included all significant thermal ions into our considerations. These values of $v_{{\rm lim},i}$, based on an arbitrary choice of $[dn_i/dv_z]_{\rm lim}$, have been defined for illustrative purpose only; the actual extent of the damping depends on the physical conditions and will be estimated later in this paper. The resulting "damping ranges" for the various ions (Fig. 4), while based on these somewhat arbitrary values of $v_{{\rm lim},i}$, are rather insensitive to the value of the chosen cutting level $[dn_i/dv_z]_{\rm lim}$, since the Maxwell distribution is sharply cut off toward higher velocities (Fig. 2).

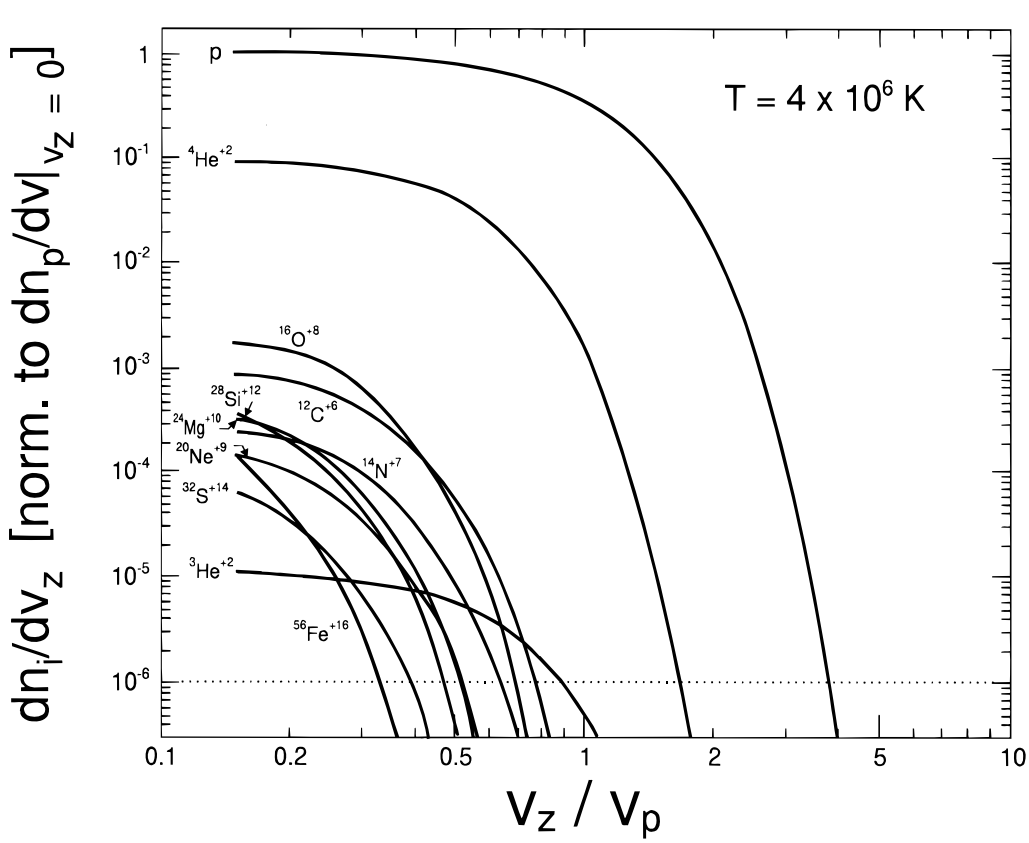

FIG. 2.—Maxwell velocity distribution dn_i/dv_z for the ion velocity component $v_z = v\mu$ along the field direction, for the most important ions in a solar active region plasma of temperature $T = 4 \times 10^6$ K with coronal composition. An isotropic distribution of the particle pitch angles is assumed, and only the positive v_z side is shown. The ordinates are normalized to the proton differential density at $v_z = 0$, $dn_p/dv_z|_{v_z=0}$, and the abscissas to the most probable proton velocity v_p. The dotted line, placed conveniently at a differential density of $[dn_i/dv_z]_{\rm lim} = 10^{-6} \times dn_p/dv_z|_{v_z=0}$, allows us to define a limiting speed $|v_z| = v_{{\rm lim},i}$ for "significant" wave damping by each particular ion i; it yields an illustrative wave damping region by each ion i in the (ω-k) plane (Fig. 4).

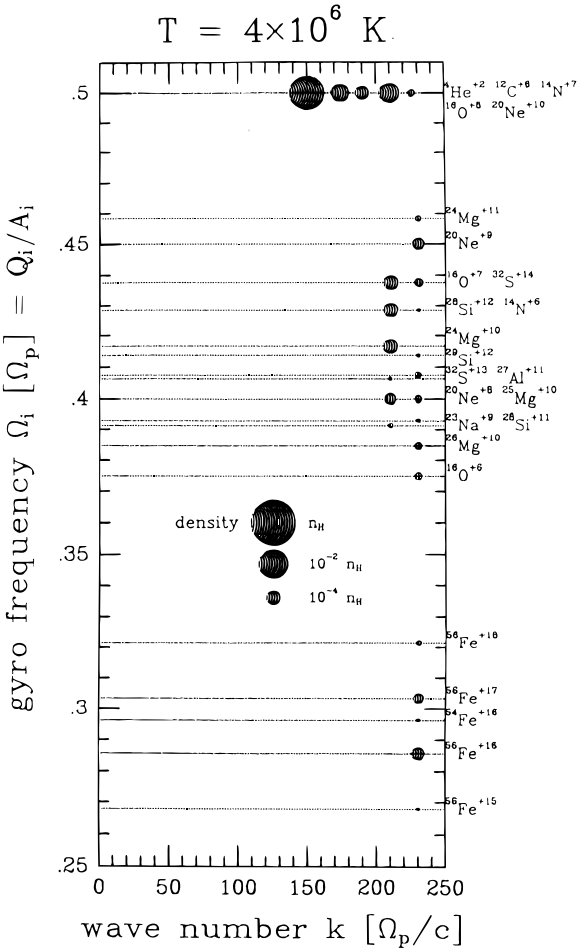

FIG. 3*a*

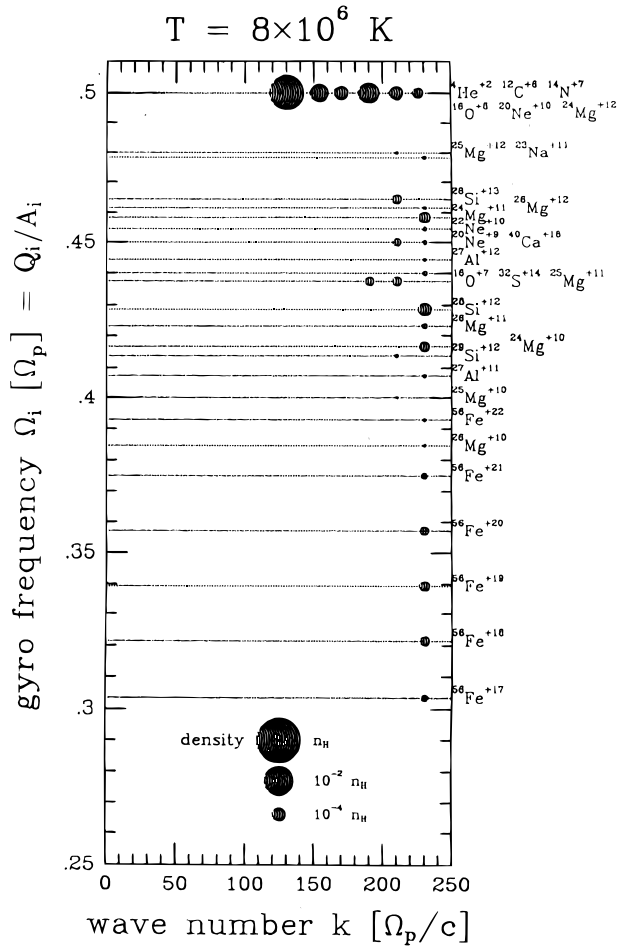

FIG. 3*b*

FIG. 3.—Gyrofrequencies Ω_i of all important ions i in solar coronal plasmas of temperature $T = 4$, 8, and 16×10^6 K ([*a*], [*b*], and [*c*], respectively), normalized to the proton gyrofrequency Ω_p. The ratio Ω_i/Ω_p is equal to the ion's charge-to-mass ratio Q_i/A_i. The size of the circles indicates the relative densities of the ion species on a logarithmic scale.

Three parameters determine the location and extension of the ion's damping region in the (ω-k) plane: the ion gyrofrequency, its abundance, and the temperature (both through the width of the Maxwell distribution and through its bearing on the ionic abundances). To illustrate the location of the gyrofrequencies of the relevant ions in a typical solar AR or flare plasma, we have plotted in Figure 3 the gyrofrequencies $\Omega_i/\Omega_p = Q_i/A_i$ of all significant ions with charge Q_i and atomic mass number A_i for three temperatures $T = 4$, 8, and 16×10^6 K. The size of each circle reflects the density of the ion species in the coronal gas on a logarithmic scale (Appendix B). For increasing temperatures, all gyrofrequencies move upward toward $\Omega_i/\Omega_p = Q_i/A_i = 0.5$, the value for fully stripped isotopes with $A = 2Z$, where Z is the nuclear charge.

The resulting damping regions for all significant ions in a coronal plasma of temperature 4×10^6 K are shown in Figure 4. The picture allows a clear subdivision into different regions. At low frequencies $\omega \sim 0.26$–$0.33\ \Omega_p$, existing wave modes undergo damping by thermal Fe. After a gap, partially ionized ions from O to S form a region around $\omega \sim 0.37$–$0.47\ \Omega_p$, where thermal damping can be due to interaction with multiple species, especially for larger wavenumbers. Around $\omega = 0.50\ \Omega_p$, very abundant $^4He^{+2}$, as well as fully stripped ions from C to Ne, gives rise to a broad range of thermal damping.

In this simple picture, the bulk density of each ion has been used to assess the approximate limits of the damping regions in the (ω-k) plane. But within these regions, the actual magnitude of the damping increases as the gyrofrequency ω moves toward the center of the damping region ($\omega/\Omega_p = Q_i/A_i$) in the ($\omega$-$k$) plane (Fig. 4). As $\omega/\Omega_p \rightarrow Q_i/A_i$, indeed, particles with smaller and smaller velocity component $|v_z|$ along the field direction fulfill the resonance condition (1). In view of the shape of the Maxwell velocity distribution (Fig. 2), these particles are more and more numerous, and hence the damping is more and more efficient as $\omega/\Omega_p \rightarrow Q_i/A_i$. The damping also increases as one considers larger and larger wavenumbers k, for a fixed frequency ω/Ω_p not too close to Q_i/A_i. Equation (1), indeed indicates that for increasing k at a fixed $\omega/\Omega_p \neq Q_i/A_i$, the waves interact with ions with smaller and smaller $|v_z|$ values, which are more and more numerous (Fig. 2).

To illustrate these important effects, we have plotted in Figure 5, in arbitrary units, the inverse number density D^{-1} of the thermal particles that are able to interact with a wave at each particular point of the (ω-k) plane, for the region close to the $^4He^{+2}$ gyrofrequency. This density has been

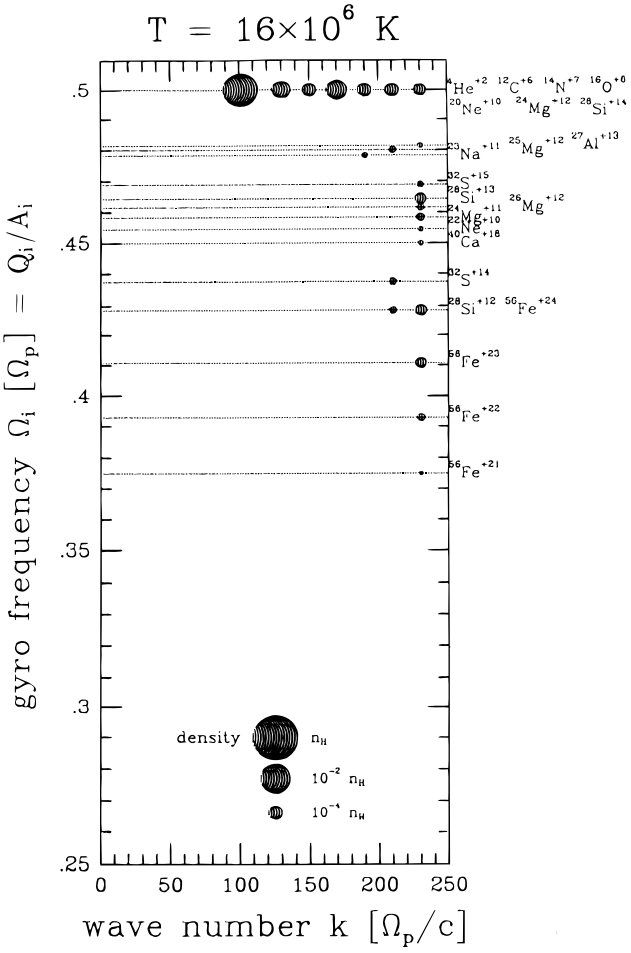

FIG. 3*c*

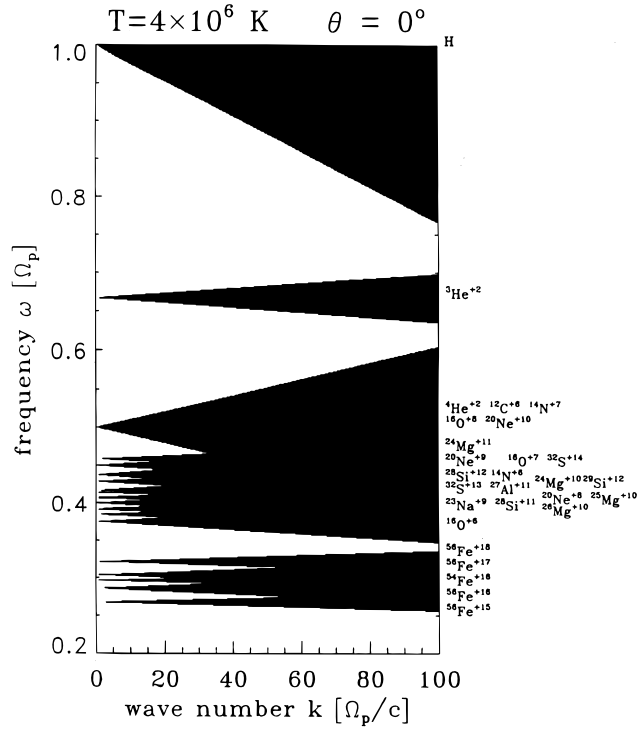

FIG. 4.—The shaded regions in the (ω-k) plane give a qualitative image of the "damping ranges" of parallel waves, over which these waves are effectively damped by interaction with the various ions present in a plasma with coronal composition and a temperature of $T = 4 \times 10^6$ K (see Fig. 3*a*). The exact width of these ranges is somewhat arbitrary, related to the values of $v_{\mathrm{lim},i}$ derived for the arbitrary cut at $[dn_i/dv_z]_{\mathrm{lim}} = 10^{-6} \times dn_p/dv_z|_{v_z=0}$ in the Maxwellians shown in Fig. 2. The broad damping ranges due to very abundant protons and $^4\mathrm{He}^{+2}$ are conspicuous, as well as the narrower ranges due to the rare $^3\mathrm{He}^{+2}$ and the two blends due to the narrow ranges of many ions of elements between N and S and to the various Fe ions.

calculated assuming an isotropic pitch angle distribution of the thermal particles, for a temperature of 4×10^6 K. As a prominent result, we notice the deep "helium valley," where interaction with thermal $^4\mathrm{He}^{+2}$ leads to strong wave damping. Among the other ions between $\omega/\Omega_p = 0.4$ and 0.5, only the three more abundant $^{16}\mathrm{O}^{+7}$, $^{28}\mathrm{Si}^{+12}$, and $^{24}\mathrm{Mg}^{+10}$ form visible smaller valleys in the "damping landscape" of this plasma (for relative abundances, see Appendix B and Fig. 3*a*).

Above the $^4\mathrm{He}^{+2}$ gyrofrequency, thermal protons form an even broader range of thermal damping around $\omega = \Omega_p$ (Fig. 4). In this frequency range, none of the heavy ions can interact with waves for moderate kc/Ω_p (at least through the first harmonics of their gyrofrequency, which is the only important one for moderately oblique waves). Only $^3\mathrm{He}^{+2}$, which has a very low abundance, can. Due to its low mass, in addition, it has a comparatively high thermal velocity, which leads to a broad interaction range. Therefore, we do not expect large wave damping rates due to interaction with $^3\mathrm{He}^{+2}$. So, only interaction with the fastest thermal protons and $^4\mathrm{He}^{+2}$ ions in the tail of the Maxwellian can significantly damp moderately oblique waves in the $^3\mathrm{He}^{+2}$ frequency region.

2.2. *Hot Plasma Dispersion Relation for Parallel Waves in a Multi-Ion Solar Coronal Plasma*

After having examined the regions of the (ω-k) plane in which wave damping might occur, we turn now to the question of which types of plasma modes are allowed in a realistic hot solar AR or flare plasma, and how these modes are damped by the background particles. We start by presenting the results of our calculations of the hot multi-ion plasma dispersion relation for parallel waves. The formula for this dispersion relation is given, e.g., in Swanson (1989, p. 158) for the case of a plasma without drifts and no anisotropic temperature effects, as

$$\frac{k^2c^2}{\omega_c^2} = 1 + \sum_j \frac{\omega_{pj}^2}{\omega_c k v_j}\left[\left(\frac{1 \pm \epsilon_j}{2}\right)Z(\zeta_{1j}) + \left(\frac{1 \mp \epsilon_j}{2}\right)Z(\zeta_{-1j})\right]. \tag{2}$$

The upper (lower) sign corresponds to R (L) waves, ω_{pj} is the plasma frequency of species j, and ϵ_j is the charge sign. The plasma dispersion function is defined as

$$Z(\zeta) = \frac{1}{\sqrt{\pi}} \int_{-\infty}^{+\infty} \frac{e^{-\xi^2}\, d\xi}{\xi - \zeta}, \tag{3}$$

with the argument $\zeta_{nj} = (\omega_c + n\Omega_j)/(kv_j)$ and $n = \pm 1$ for the parallel case.

We note that in the case of weak turbulence equation (2) is valid only if the gyroresonance condition (1) is fulfilled exactly. For strong turbulence, however, waves and particles will interact in the strong damping region even if gyrofrequency and Doppler-shifted wave frequency fulfill only approximately the gyroresonance condition. Hence, our results will underestimate the energy exchange between

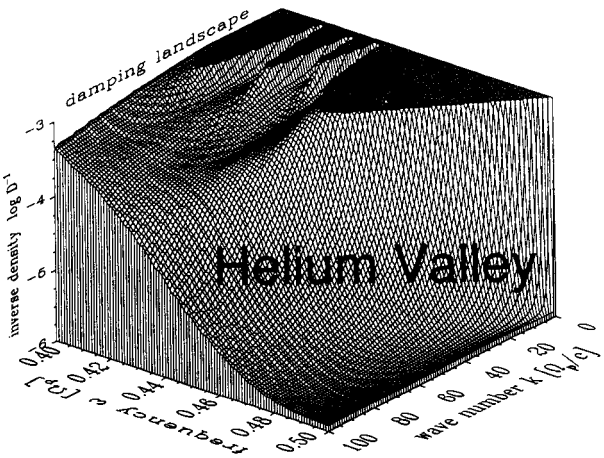

FIG. 5.—The inverse density D^{-1} of those thermal particles that are able to interact with waves for each point in the (ω-k) plane, for a temperature of $T = 4 \times 10^6$ K (arbitrary units). It illustrates the "damping landscape" for wave frequencies close to $\Omega_{^4He^{+2}}$. Most of the thermal damping is due to interaction with thermal $^4He^{+2}$, forming a deep helium valley. Much shallower additional damping valleys due to $^{16}O^{+7}$, $^{28}Si^{+12}$, and $^{20}Mg^{+10}$ are visible. The shape of these valleys is a direct reflection of the Maxwell distribution for the ion's velocity component v_z along the magnetic field direction, shown in Fig. 2.

waves and particles in the strong damping region. This additional effect will be dealt with in a forthcoming paper.

With all the ion species contributing at different frequencies, the task of finding the values of k and $\omega_c = \omega - i\omega_{\rm im}$ by solving equation (2) requires advanced numerical methods. We used Muller's method to find the roots in the complex plane and three different criteria to calculate Z (see, e.g., Press et al. 1990).

Examples of the resulting, complete dispersion relation will be shown in Figure 10. But we found it useful to illustrate first its characteristic behavior over specific frequency ranges in Figures 6–9. To describe the complex function $\omega_c(k)$ in these figures, we show in the top panels the (ω-k) plane, i.e., the conventional dispersion relation, and in the bottom panels directly the (τ_d-k) plane, where $\tau_d = 1/\omega_{\rm im}$ is the damping timescale, i.e., the time in which the wave amplitude is decreased by a factor $1/e$.

Figure 6 is devoted to the dispersion relation and damping near the gyrofrequencies of the rarer $^{56}Fe^{+15}$ and of the neighboring, dominant $^{56}Fe^{+16}$ ion, for a temperature of 4×10^6 K (abundance ratio: $^{56}Fe^{+15}/^{56}Fe^{+16} = 6/100$). In the top panel, the thin dotted lines give the gyrofrequencies of these ions, and the large dots represent their density (see Fig. 3). The thin short-dashed lines indicate the limits of the damping regions associated with these ions, as discussed above (see Fig. 4; § 2.1).

For the real part of the frequency, the solid line is the continuation of the L-wave Alfvén dispersion relation starting at the origin. This mode encounters damping when ω enters the damping region of $^{56}Fe^{+15}$ at $kc/\Omega_p \sim 47$. The other L mode, represented by long dashes, starts at $k = 0$ slightly above $\omega = \Omega_{^{56}Fe^{+15}}$. For very small values of kc/Ω_p, the mode lies outside the $^{56}Fe^{+15}$ damping range and cannot be damped by any particles, since $|\omega - (\Omega_i/\gamma)| \gg kv_z$ when $k \to 0$; this holds for both nonrelativistic and relativistic particles. Beyond $kc/\Omega_p \sim 1$, it enters this damping range and rapidly becomes more and more damped. The damping still increases as the mode moves along to increasing k while keeping near the center of the widening $^{56}Fe^{+15}$ valley, since the waves then interact with ions with smaller and smaller $|v_z|$. Beyond $kc/\Omega_p \sim 48$, the mode moves upward and reaches a little "corner" left by the damping regions of $^{56}Fe^{+15}$ and $^{56}Fe^{+16}$, where only the few very fast thermal particles of the corresponding Maxwellian tails can interact with the waves. Hence, weak damping occurs for waves up to $kc/\Omega_p \sim 52$. For larger k values, the dashed mode becomes a $^{56}Fe^{+16}$ cyclotron mode undergoing strong damping.

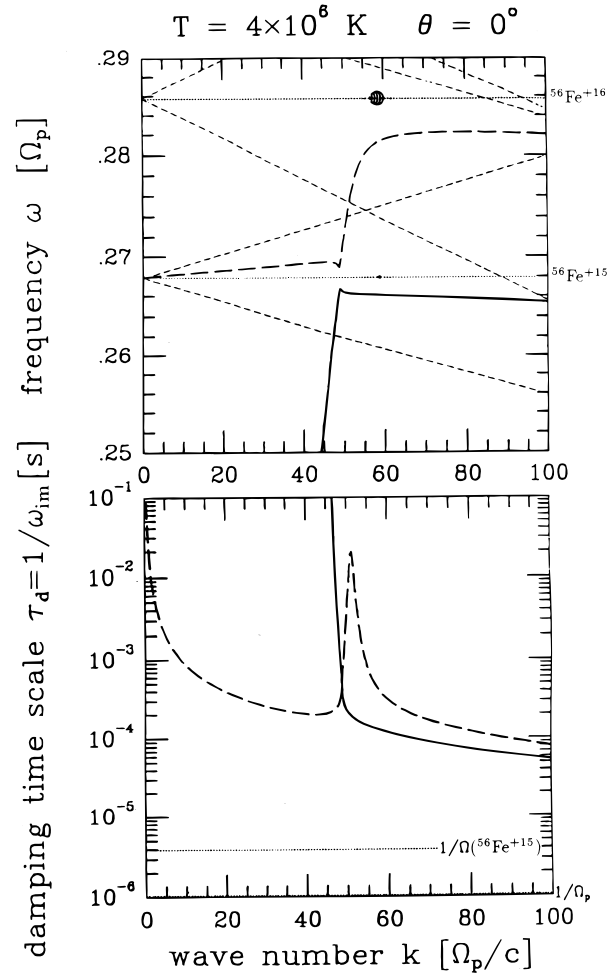

FIG. 6.—Dispersion relation (*top*) and damping timescales (*bottom*) of parallel left polarized plasma waves in a multi-ion hot active region plasma at $T = 4 \times 10^6$, for frequencies close to the rare $^{56}Fe^{+15}$ and the more abundant $^{56}Fe^{+16}$ gyrofrequencies. In the top panel, the dotted lines indicate the gyrofrequencies of both ions, the short-dashed lines limit the corresponding ranges of strong thermal damping, and the heavy solid and long-dashed lines represent the wave modes; the size of the circles indicates the relative densities of the ion species. In the lower panel, the damping timescales of both modes are shown, along with the time a $^{56}Fe^{+15}$ ion and a proton take to complete one gyration (*dotted lines*) ($n_e = 10^{10}$ cm^{-3}, $B = 100$ G).

In this way, we qualify our preliminary considerations about the damping range as valuable for a detailed understanding of the wave damping in the hot multi-ion plasma. Just from the upper picture in conjunction with the plotted damping regions, we would expect an increase in the damping timescale for the long-dashed mode around $kc/\Omega_p = 50$, and the exact calculation using the imaginary part of the frequency confirms this expectation.

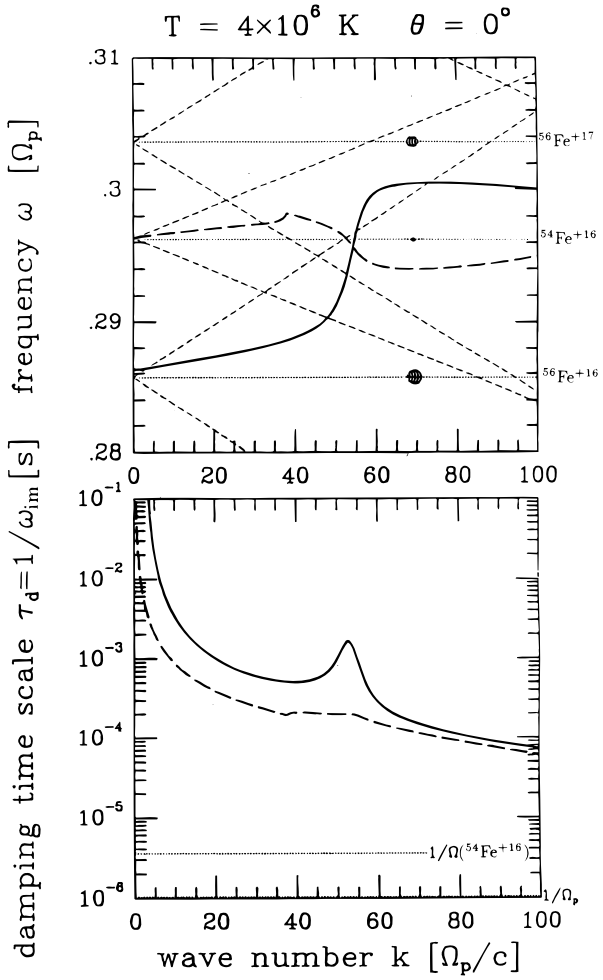

FIG. 7.—Same as Fig. 6, for frequencies close to the gyrofrequencies of the abundant $^{56}Fe^{+16}$, the rare $^{54}Fe^{+16}$, and the abundant $^{56}Fe^{+17}$.

At this point, the question arises why the $^{56}Fe^{+15}$ cyclotron waves (solid mode at $kc/\Omega_p > 60$) undergo slightly stronger damping than the $^{56}Fe^{+16}$ cyclotron waves (long-dashed mode), in spite of the small density ratio $n(^{56}Fe^{+15})/n(^{56}Fe^{+16}) = 1/17$. One might argue that the $^{56}Fe^{+15}$ cyclotron waves penetrate deeper into the $^{56}Fe^{+15}$-Maxwell distribution than the $^{56}Fe^{+16}$ waves into their corresponding distribution. But the main reason for this strong damping of waves by a low abundant component of the plasma is an effect called "comoving gyroresonance." In SM, this process was identified for the case of electron-Whistler interaction, when the projection of the electron velocity on the direction of the ambient magnetic field is nearly equal to the group speed v_g of the parallel propagating Whistler waves. The effect is directly visible, e.g., in the Fokker-Planck coefficients describing the momentum change of the charged particles due to gyroresonant interaction (for electrons, see SM, eqs. [3.12] and [3.18]):

$$D_{pp}(\mu, p) \sim |v\mu - v_g|^{-1} . \quad (4)$$

For $v\mu = v_z \approx v_g$, the denominator is small and the wave energy is effectively transferred from the waves to the particles, since the waves transport energy with the same speed as the gyration center moves along the magnetic field. In the present case of the interaction between low-frequency cyclotron waves and rare heavy ions, the interaction becomes more efficient when a mode lies close to an ion's gyrofrequency and has $v_z \approx v_g$. This is the case for the $^{56}Fe^{+15}$ cyclotron mode (*solid line*), but not for the $^{56}Fe^{+16}$ cyclotron mode (*long-dashed line*). So, the $^{56}Fe^{+15}$ ions with $v_z \approx v_g$ are able to pick up easily all the wave energy in a short timescale via comoving gyroresonance.

The general influence of the $^{56}Fe^{+15}$ and $^{56}Fe^{+16}$ ions on the "undisturbed" dispersion relation of an *e-p*-He plasma can be described as a split of the main mode in the vicinity of the gyrofrequency, with a divergence of k (see Fig. 1). But the strength of the disturbance depends on the abundances, and Figure 6 does show that the dispersion relation is distorted much less by the splitting near the gyrofrequency of rare $^{56}Fe^{+15}$ than near that of abundant $^{56}Fe^{+16}$. This will also be illustrated in the next example.

Above the gyrofrequency of dominant $^{56}Fe^{+16}$, we find the two neighboring gyrofrequencies of the rare isotope ion $^{54}Fe^{+16}$ and of the more abundant $^{56}Fe^{+17}$ (abundance ratios: $^{56}Fe^{+16}/^{54}Fe^{+16}/^{56}Fe^{+17} = 100/6/51$) (Fig. 7). The first mode (*solid line*) starts above the $^{56}Fe^{+16}$ gyrofrequency and suffers strong damping in the damping region of $^{56}Fe^{+16}$, until it finds a "corner" between the damping regions of $^{56}Fe^{+16}$ and $^{56}Fe^{+17}$ at $kc/\Omega_p \sim 55$, similar to the one described in Figure 6. Here the damping timescale

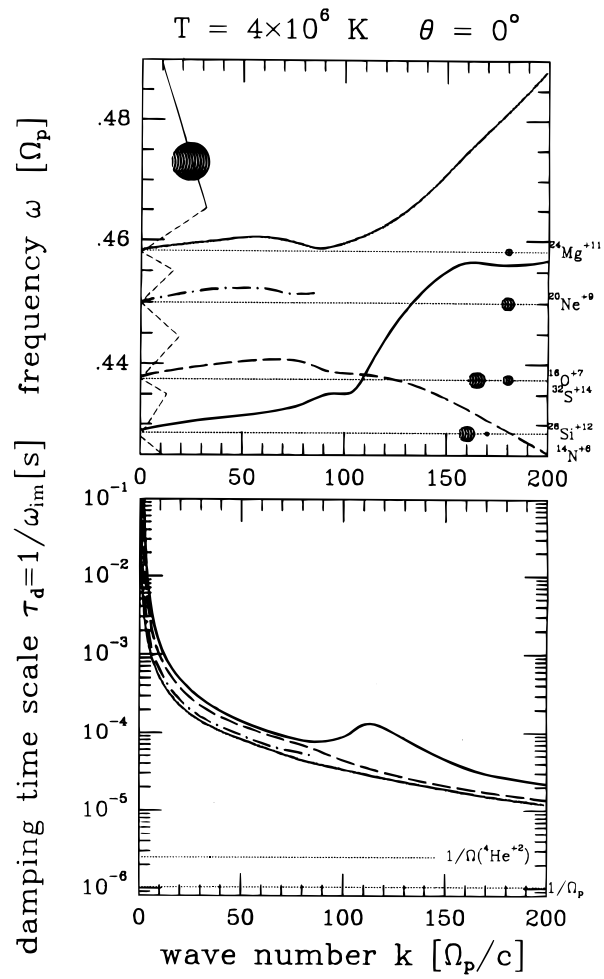

FIG. 8.—Same as Fig. 6, for frequencies in an interval close below the $^{4}He^{+2}$ gyrofrequency, showing the predominant role of the damping by $^{4}He^{+2}$, and the intricate mode splitting due to various minor ions of elements between N and S.

in the "corner" does not rise as much as in Figure 6, since the mode never really leaves the damping regions of $^{56}Fe^{+16}$ and $^{56}Fe^{+17}$. In addition, the mode is then located right in the damping range of the rare isotope ion $^{54}Fe^{+16}$, so that some damping is expected from this rarer species as well. With still increasing k, the mode passes into the damping region of the more abundant $^{56}Fe^{+17}$, and the damping timescale decreases again.

The second mode in Figure 7 (*long-dashed line*) never escapes the $^{54}Fe^{+16}$ damping region, and in addition it suffers strong damping by the thermal $^{56}Fe^{+16}$ and $^{56}Fe^{+17}$ ions at larger values of kc/Ω_p. An interesting point to note is that for $kc/\Omega_p \approx 55$ the real parts of the dispersion relation $\omega(k)$ of both modes intersect, while the damping rates differ by an order of magnitude. This means that, although both waves have the same wavenumber and frequency and hence interact with the same particles, they suffer different dampings. This reflects directly the above-mentioned effect of comoving gyroresonance of cyclotron waves.

For illustration only, we add another example of a region with dense lying gyrofrequencies close to the $^4He^{+2}$ gyrofrequency. Figure 8 shows the different L modes in the frequency interval [0.425–0.490 Ω_p]. It is hard to follow the modes through the complicated pattern of the damping regions. All modes in this region undergo heavy damping, on timescales $<10^{-3}$ s for $kc/\Omega_p > 15$, due mainly to $^4He^{+2}$ (see solid thin line starting at the point [0, 0.50]).

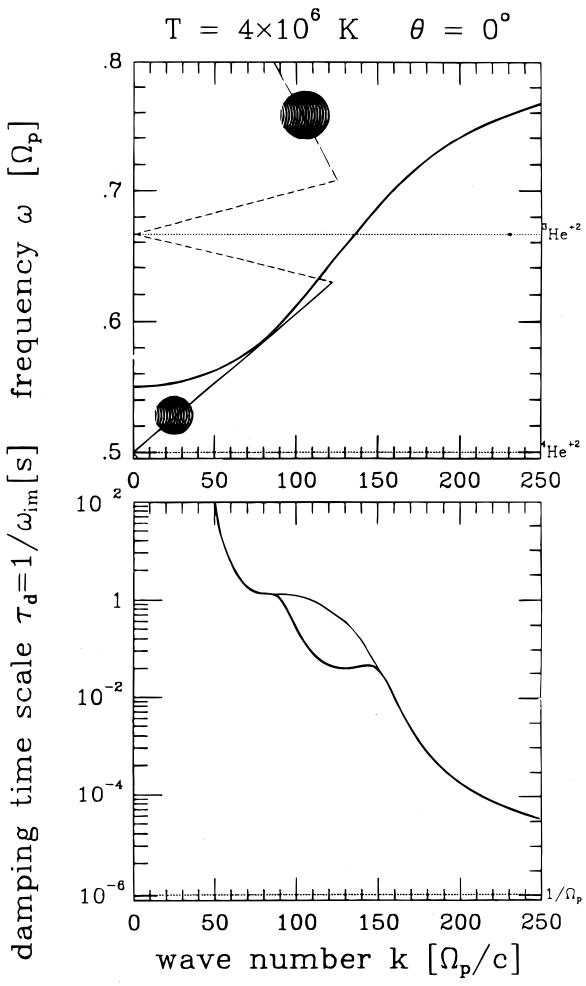

FIG. 9.—Same as Fig. 6, for frequencies around the $^3He^{+2}$ gyrofrequency, i.e., between the $^4He^{+2}$ and the proton gyrofrequencies.

It is, on the contrary, very illuminating to study the range between $\omega = 0.5\ \Omega_p$ and Ω_p, shown in Figure 9. Here the L-wave dispersion relation is determined mainly by H^+, $^4He^{+2}$, and $^3He^{+2}$. In the light of the huge enhancements of the ^3He isotope usually observed in impulsive flare-accelerated particles, this region is of considerable importance, and the results will be discussed in the conclusions. The real part of the dispersion relation starts for small k above $\omega/\Omega_p = 0.55$ and suffers slight damping by the fastest thermal $^4He^{+2}$ ions because it approaches the $^4He^{+2}$ damping range without entering it completely. Consequently, the damping timescale shows a slight valley with a minimum at $kc/\Omega_p \sim 80$. For large k values, we expect strong damping by thermal protons starting at $kc/\Omega_p \sim 145$, and the damping timescale indeed shows a steep decrease above this value.

The thin solid line in the lower picture represents the timescale for damping due to protons and $^4He^{+2}$ only. The complete thick solid line, however, reveals the thermal damping by $^3He^{+2}$ as a shallow valley with minimum at $kc/\Omega_p \sim 130$, where the dispersion relation penetrates the damping range of this isotope.

Again, the low abundance of $^3He^{+2}$ prevents a splitting of the dispersion relation. But, due to both their low mass and the absence of other ions with nearby gyrofrequencies, the thermal $^3He^{+2}$ ions will suffer efficient acceleration by a range of waves, which is somewhat broader than the corresponding acceleration ranges for all heavy ions with gyrofrequencies below $kc/\Omega_p = 0.5$. We will investigate this situation in a forthcoming paper, but we predict at this point that the hotter the plasma, the less efficient the acceleration of $^3He^{+2}$. From Figure 9, we can, indeed, see that with increasing temperature the thermal regions of both $^4He^{+2}$ and protons will broaden, leaving no space for the "corner," in which mainly thermal $^3He^{+2}$ ions can interact with the waves. From preliminary calculations, we find that for high temperatures $T > 6 \times 10^6$ K preferential acceleration of $^3He^{+2}$ by non–quasi-perpendicular waves is impossible.

2.3. *Dynamic Damping of Waves*

We are now in a position to answer the following question: What will happen to parallel waves which are injected at an arbitrary frequency in an environment like the solar AR plasma? In the following, we will restrict ourselves to the case in which the damping of the waves does not lead to a substantial change in the overall plasma temperature on the considered timescales. Of course, our analysis is able to treat the other case as well. We would then have to start at a given temperature, calculate the wave spectrum after a short time, as well as the energy of the background particles gained by the damping, and then proceed with the new temperature. However, for the purpose of investigating whether or not parallel wave damping in gyroresonant acceleration models could in principle account for the observed abundances, we will restrict ourselves to first-order considerations.

To obtain a picture of the waves available for interaction with the different ion species as a function of the time Δt elapsed since wave injection (assumed instantaneous), we show in Figure 10 the real part of the frequency of all waves, which have not yet been damped by thermal particles after

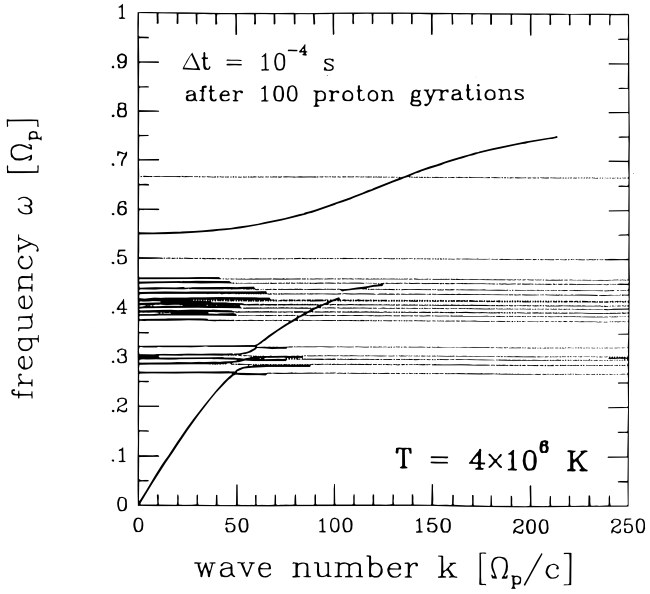

FIG. 10*a*

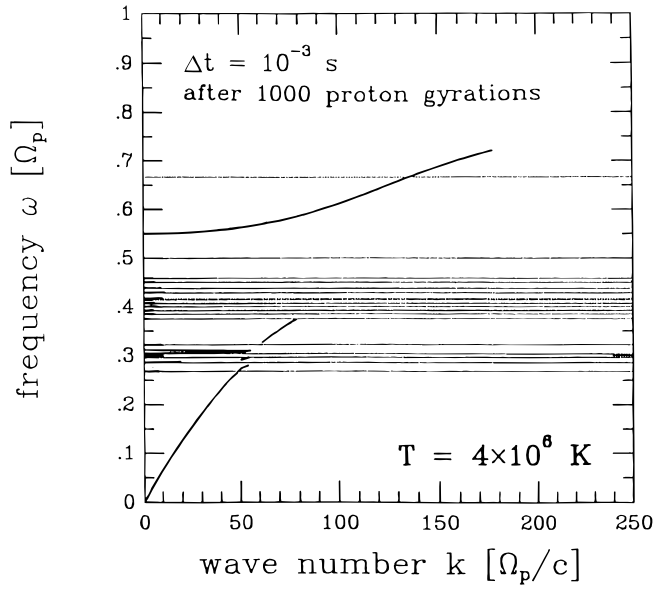

FIG. 10*b*

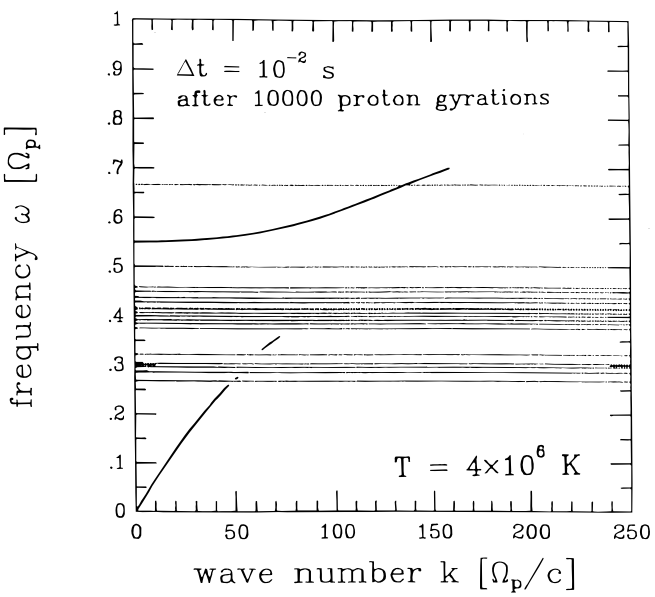

FIG. 10*c*

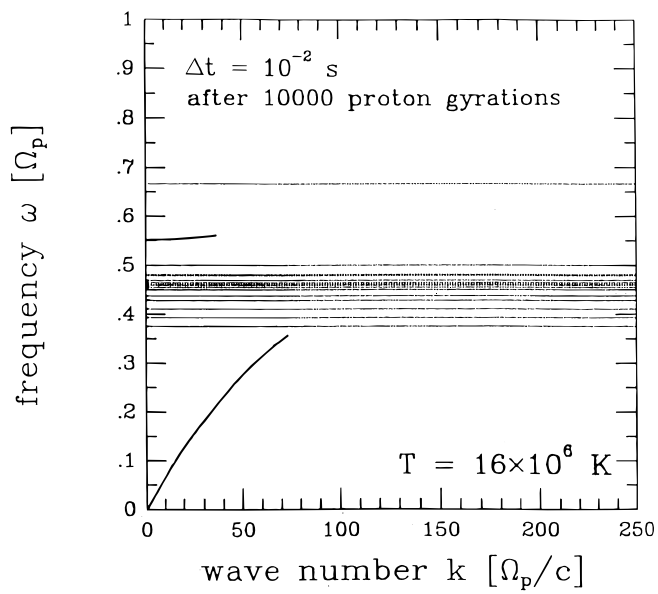

FIG. 10*d*

FIG. 10.—Complete multi-ion plasma dispersion relation for parallel waves in a solar active region plasma. The relation is plotted only in regions in which the waves have not been substantially damped after a time of Δt ($n_e = 10^{10}$ cm^{-3}, $B = 100$ G). (*a*–*c*) The relation for $T = 4 \times 10^6$ K and $\Delta t = 10^{-4}$, 10^{-3}, and 10^{-2} s, respectively. The relation for a higher plasma temperature of $T = 16 \times 10^6$ K and $\Delta t = 10^{-2}$ is shown in (*d*).

Δt and are thus still available to preferentially accelerate ions. To do so, we interrupt the plotting of the dispersion relation where the *e*-folding damping timescale τ_d falls below the given time interval Δt. Possible other interpretations of Δt will be discussed in § 4.2.

We start with Figure 10*a* for a temperature of 4×10^6 K and $\Delta t = 10^{-4}$ s, which corresponds to the time it takes a proton to perform 100 gyrations in a field of $B = 100$ G. By and large, we obtain the shape of the cold plasma dispersion relation of the *e*-*p*-He plasma (see Fig. 1), now disturbed by the ion resonances. Clearly visible, thermal damping by protons and $^4He^{+2}$ ions is the dominant mechanism leading to cutoffs in the proton and $^4He^{+2}$ cyclotron ranges. Most of the low-*k*, high phase speed waves at $\omega/\Omega_p < 0.5$ still exist and are available for heavy ion acceleration.

Figures 10*b* and 10*c* illustrate the evolution of the wave spectrum after longer times. After 10^{-3} s, most of the low-*k*, high phase speed waves at $\omega/\Omega_p < 0.5$ have been damped by interaction with heavy ions, and the He cyclotron waves beyond $kc/\Omega_p = 80$ have been damped by interaction with $^4He^{+2}$. After 10^{-2} s, all ion high phase speed waves are gone, the $^4He^{+2}$ cyclotron waves are even more damped, and the proton cyclotron waves, damped by protons, exist only up to approximately the $^3He^{+2}$ gyrofrequency. The Alfvén range is not affected.

Increasing the temperature has two effects. They are illustrated in Figure 10*d*, which shows, as an extreme example,

the dispersion relation after 10^{-2} s for $T = 16 \times 10^6$ K. First the gyrofrequencies of the heavy ions have moved up toward $\Omega_i/\Omega_p = 0.5$ (§ 2.1; Fig. 3). As a result, the range of unperturbed Alfvén waves extends now to somewhat higher frequencies. Second, all thermal damping regions have broadened. There are no longer any heavy ion high phase speed waves, nor any cyclotron waves of any kind. Even the proton high phase speed waves have been suppressed completely by interaction with $^4He^{+2}$ (see Fig. 9. Even $^3He^{+2}$ can no longer be accelerated.

To sum up, acceleration of thermal ions will take place near their gyrofrequency. Whether waves are able to accelerate a particular ion species out of the thermal distribution depends on not only the injected wave intensity but also the location of its gyrofrequency with respect to those of other, abundant, ions, and on the width of the damping regions of these ions. This width is a strong function of the temperature.

3. THE GENERAL CASE OF OBLIQUE WAVES AND THE HELIUM VALLEY

The calculations in the last section have led us to the conclusion that preferential acceleration of a specific ion is possible only if the appropriate waves are not damped simultaneously by interaction with other, more abundant, ions. In the case of the scarce heavy ions, the most prominent candidate for this damping is $^4He^{+2}$ because it can reach the resonance region of the heavier ions for the temperatures relevant to ARs and flares. The limits of this "Helium Valley," which places a serious constraint on any heavy ion acceleration model, though, can be determined by a calculation considering only a hot *e-p*-He plasma, which is much simpler than the multi-ion calculation presented in the last section.

This allows us to generalize our treatment on one point: we can study the entire class of waves, propagating at an arbitrary angle θ with respect to the magnetic field direction. The importance of this generalization can be illustrated by considering the resonance condition for oblique waves propagating at an angle θ to the magnetic field,

$$\omega = kv\mu \cos\theta + \frac{n\Omega}{\gamma} . \tag{5}$$

In § 2.1, we found that this type of equation yields approximate limits to the thermal damping range in the (ω-k) plane: the two straight lines we obtained by choosing for $|v_z|$ some limiting speed $v_{\mathrm{lim},i}$ in the tail of the Maxwell distribution for the ion velocity component along the field direction. But for oblique waves, we find an additional factor $\cos\theta$ in the slope of the line, leading to an essential reduction of the interaction range of each species for nonvanishing θ. This implies that waves with large angles θ will interact with thermal particles only in a narrower frequency range around the corresponding gyrofrequency, and that especially the He valley will shrink with increasing θ. This effect will be drastic for nearly perpendicular waves. Hence, it seems necessary to study this larger class of waves in order to decide whether the He valley plays a major role in explaining the observed abundances of impulsive flare energetic particles in the framework of a gyroresonant acceleration model.

When we generalize to oblique waves, the $\cos\theta$ factor is, however, not the only change in the conditions of the interaction. Four additional changes are relevant: (i) The polarization of the modes is modified. Parallel waves have clearly distinguished circularly polarized right and left modes. Oblique waves are elliptically polarized, containing a mixture of both polarizations, with a tendency to linear polarization for high θ. (ii) The dispersion relation is modified, so that the group and the phase speed are a function of θ. (iii) Some modes decouple (see Fig. 11). These three points are described in detail in Appendix C for the simple case of oblique waves in a cold *e-p*-He plasma, and we will use these results in interpreting our hot plasma results. (iv) Finally, the gyroresonant interaction process itself becomes more complicated (see, e.g., Swanson 1989, p. 159). For oblique waves, the higher order resonances $n \neq \pm 1$ start to contribute more and more with increasing angle, and the Cerenkov resonance at $n = 0$ has to be considered. In conjunction with the elliptical polarization, this yields to damping of both the left and the right component of the waves due to Cerenkov resonance with protons and electrons, respectively.

In this section, we will illustrate and discuss all these combined complications, using the powerful tool offered by the hot *e-p*-He plasma dispersion relation studied in the framework of the kinetic theory.

3.1. *The Hot Plasma Dispersion Relation for Oblique Waves in an e-p-*He *Plasma*

For an arbitrary angle θ, the hot plasma dispersion relation for oblique waves without drifts and temperature anisotropies can be found, e.g., in Swanson (1989, p. 157). It can be written as

$$\begin{aligned}
&\{[k^2c^2\cos^2\theta - \omega_c^2 K_1][k^2c^2 - \omega_c^2(K_0 + K_1)] + \omega_c^4 K_2^2\}\omega_c^2 K_3 \\
&\quad + k^2c^2 \sin^2\theta\{[k^2c^2 - \omega_c^2(K_0 + K_1)]\omega_c^2 K_1 - \omega_c^4 K_2^2\} \\
&\quad + \omega_c^2 K_4[k^2c^2 - \omega_c^2(K_0 + K_1)][k^2c^2 \sin(2\theta) + \omega_c^2 K_4] \\
&\quad - \omega_c^2 K_5\{[k^2c^2 \cos^2\theta - \omega_c^2 K_1]\omega_c^2 K_5 \\
&\quad + \omega_c^2 K_2[k^2c^2 \sin(2\theta) + 2\omega_c^2 K_4]\} = 0 .
\end{aligned} \tag{6}$$

The elements of the dielectric tensor $\hat{K}$ contain infinite sums over all resonance orders,

$$K_0 = 2\sum_j \frac{\omega_{pj}^2 \lambda_j e^{-\lambda_j}}{\omega_c k \cos\theta v_j} \sum_{n=-\infty}^{+\infty} [I_n(\lambda_j) - I_n'(\lambda_j)]Z(\zeta_{nj}) , \tag{7}$$

$$K_1 = 1 + \sum_j \frac{\omega_{pj}^2 e^{-\lambda_j}}{\omega_c k \cos\theta v_j \lambda_j} \sum_{n=-\infty}^{+\infty} n^2 I_n(\lambda_j) Z(\zeta_{nj}) , \tag{8}$$

$$K_2 = i\sum_j \frac{\epsilon_j \omega_{pj}^2 e^{-\lambda_j}}{\omega_c k \cos\theta v_j} \sum_{n=-\infty}^{+\infty} [I_n(\lambda_j) - I_n'(\lambda_j)]Z(\zeta_{nj}) , \tag{9}$$

$$K_3 = 1 - \sum_j \frac{\omega_{pj}^2 e^{-\lambda_j}}{\omega_c k \cos\theta v_j} \sum_{n=-\infty}^{+\infty} I_n(\lambda_j)\zeta_{nj} Z'(\zeta_{nj}) , \tag{10}$$

$$K_4 = \frac{1}{2}\sum_j \frac{\omega_{pj}^2 e^{-\lambda_j} \tan\theta}{\omega_c \Omega_j \lambda_j} \sum_{n=-\infty}^{+\infty} n I_n(\lambda_j) Z'(\zeta_{nj}) , \tag{11}$$

$$K_5 = \frac{i}{2}\sum_j \frac{\epsilon_j \omega_{pj}^2 e^{-\lambda_j} \tan\theta}{\omega_c \Omega_j} \sum_{n=-\infty}^{+\infty} [I_n(\lambda_j) - I_n'(\lambda_j)]Z'(\zeta_{nj}) , \tag{12}$$

with the notations defined in § 2.2, and with the modified Bessel function of the first kind I_n, their derivative I_n', and the abbreviation $\lambda_j = (k^2 \sin^2\theta v_j c)/(2\Omega_j^2)$.

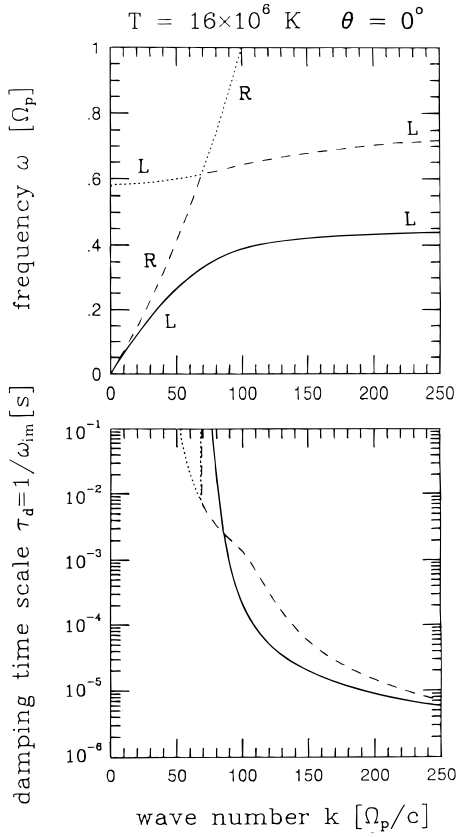

FIG. 11*a*

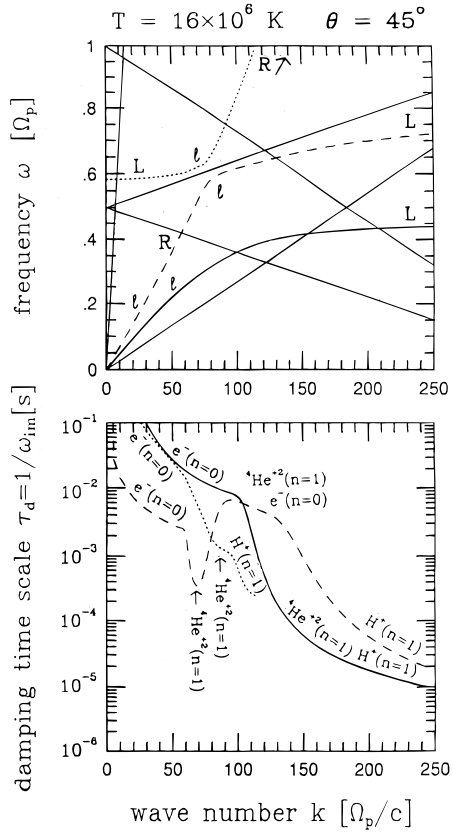

FIG. 11*b*

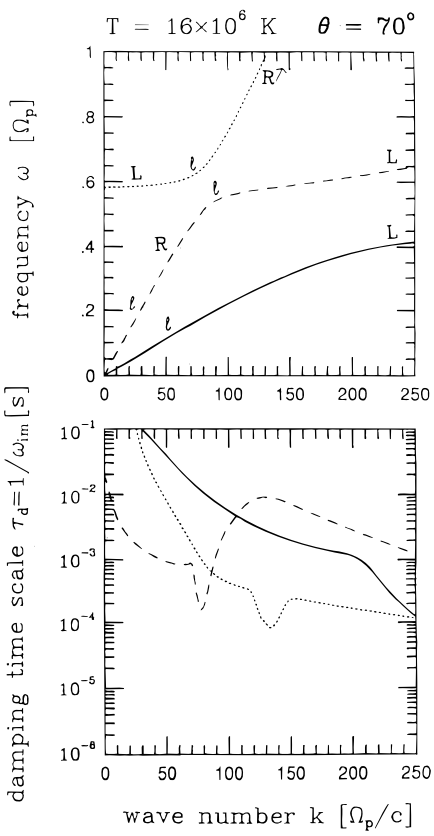

FIG. 11*c*

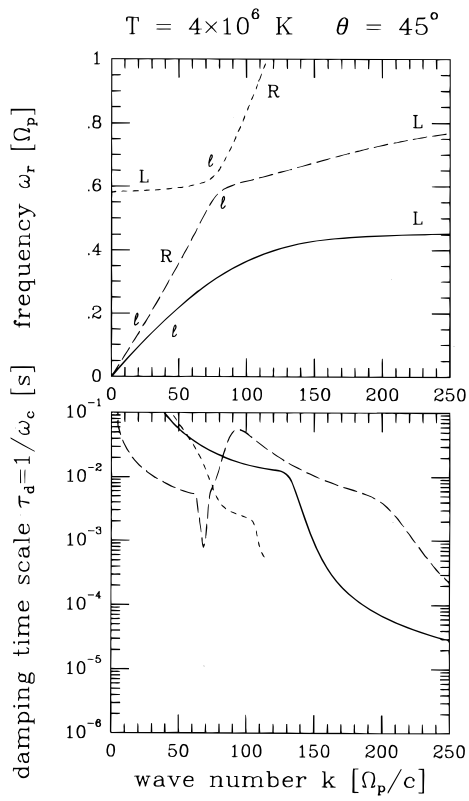

FIG. 11*d*

FIG. 11.—Complete hot plasma dispersion relation (*top*) and damping timescales (*bottom*) of waves with the propagation angle θ, for a pure *e*-*p*-He plasma. In the top panels, the three branches of the dispersion relation are represented by solid, dashed, and dotted lines; they are labeled with the approximate sense of polarization of the waves, denoted R, L, and *l* for right-hand, left-hand, and linear, respectively ($n_e = 10^{10}$ cm^{-3}, $B = 100$ G). (*a*–*c*) A hot plasma at $T = 16 \times 10^6$ K, with wave propagation angles of $\theta = 0°$ (parallel waves), 45°, and 70°, respectively. In (*b*), the damping regions (for protons $n = 0$, 1, He $n = 1$, and electrons $n = 0$) are drawn as thin solid lines in the upper panel; in the lower panel, labels indicate which plasma component and which resonance order dominates the wave damping. The relation for $\theta = 45°$ and the cooler temperature $T = 4 \times 10^6$ K is shown in (*d*).

To find the roots of the extremely complicated complex function on the left side of equation (6), we have used an algorithm based on the Muller method (see Press et al. 1990). As expected, the dispersion relation turned out to be very sensitive to the complex part of the frequency.

Resulting dispersion relations are illustrated in Figure 11, for a few specific situations. In these figures, the top panel shows the three branches of the real part of the dispersion relation (hereafter denoted "solid," "dashed," and "dotted" modes), with the predominant left- or right-circular polarization of the waves indicated. The regions in which the modes are predominantly linearly polarized are labeled with an *l*. The associated damping timescales τ_d are shown in the bottom panels. Note that the damping of the left and right components of the waves by ions and electrons, respectively, are independent (§ 2.1). However, the damping times τ_d yielded by the general dispersion relation (6) refer to the amplitude of the mixed polarized waves. So when τ_d is short due to the interaction of the R component with the electrons, the left component may still be weakly damped.

Figures 11*a*–11*c* depict the change of the dispersion relation for increasing angle θ, for a fixed temperature $T = 16 \times 10^6$ K. Although the temperature of the relevant solar plasma is probably lower, we chose the higher temperature case to be discussed in more detail for illustrative purpose, since the damping effects are more prominent in this case. Figure 11*d* will illustrate the more realistic case $T = 4 \times 10^6$ K, for $\theta = 45°$.

To relate this treatment to our results of § 2, we start in Figure 11*a* with the dispersion relation and damping timescales for $\theta = 0°$ and $T = 16 \times 10^6$ K. This figure (*top*) is similar to Figure 1. The "dashed" and "dotted" modes (so plotted in analogy with the subsequent figures) touch at the "point of contact" near $kc/\Omega_p \sim 70$, as in Figure 1, and all waves are purely left or right polarized. The waves cannot interact with electrons for $n = 0$, which prevents any damping of all right-polarized modes (the $n = 1$ electron resonance lies at large $\omega/\Omega_p \approx 1836$). The left-polarized "solid" mode is damped only for $kc/\Omega_p > 80$, as it enters the $^4He^{+2}$ damping region. At lower k values, before the point of contact, the L-polarized "dotted" mode shows the onset of a decrease of τ_d, due to the interaction with the fastest $^4He^{+2}$ ions. Beyond this point, the mode becomes right polarized with $\tau_d \to \infty$. Similarly, $\tau_d \to \infty$ before the point of contact for the "dashed" right-polarized Alfvén wave branch. Later, the mode, now left polarized, just continues the trend of the lower k "dotted" mode, with a decrease of τ_d as it penetrates into the He valley and a steepening above $kc/\Omega_p \sim 100$ due to growing interaction with protons as well.

In Figure 11*b*, we present the dispersion relation and damping timescales for $\theta = 45°$ and $T = 16 \times 10^6$ K. The limits of the key damping regions introduced in §§ 2.1 and 2.3 are plotted as solid lines on the figure. As expected, new features appear for oblique propagation: the "dashed" and "dotted" modes are decoupled; the waves are now mixed polarized; finally, the $n = 0$ resonances with electrons and protons are now capable of damping the right and left components of the waves, respectively, and therefore they have to be considered. Starting at the proton gyrofrequency, $\omega/\Omega_p = 1$, the delimiting line of the proton ($n = 1$) damping region crosses at $kc/\Omega_p \sim 90$ the "dotted," at $kc/\Omega_p \sim 130$ the "dashed," and at $kc/\Omega_p \sim 200$ the "solid" branch of the dispersion relation. Starting at the $^4He^{+2}$ gyrofrequency, $\omega/\Omega_p = 0.5$, the delimiting lines of the $^4He^{+2}$ ($n = 1$) damping range includes for $kc/\Omega_p > 50$ the "dashed" and for $kc/\Omega_p > 100$ the "solid" branch. Starting at $\omega/\Omega_p = 0$, the delimiting line of the proton ($n = 0$) damping region includes the "solid" branch for $kc/\Omega_p > 150$. Finally, starting at $\omega/\Omega_p = 0$, the delimiting line of the extremely broad electron ($n = 0$) resonance region includes almost the entire wave range because of the high thermal speed of the electrons $v_e \approx 43 v_p$. Although unavoidably visible in the damping timescales relevant to the mixed polarized wave, this damping, due to electrons in Cerenkov resonance operating on the right component only, does not affect the preferential acceleration of ions (§ 2.1).

Having illustrated the approximate location of the damping ranges, we analyze now the resulting damping timescales τ_d, shown in the bottom panel of Figure 11*b*. First, consider the "solid" mode damping curve. For $kc/\Omega_p < 100$, there is a decrease of τ_d due to the interaction

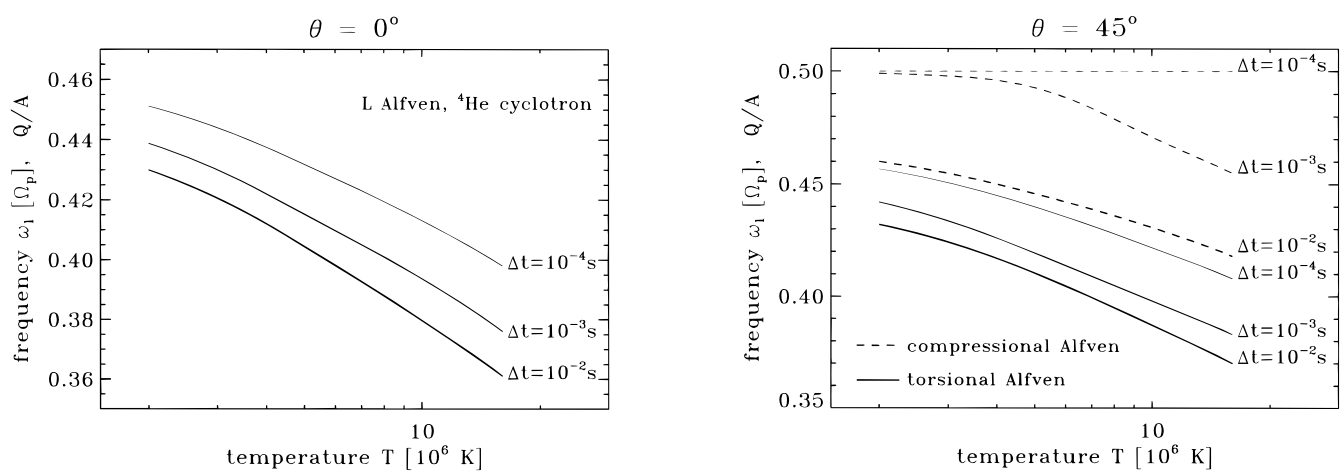

FIG. 12*a* FIG. 12*b*

FIG. 12.—Broadening of the helium valley with temperature and time: ω_l, the limiting frequency of the He valley along the dispersion relation (see Fig. 10) is shown as a function of the temperature, for three different time intervals Δt over which the waves have been subjected to damping ($n_e = 10^{10}$ cm^{-3}, $B = 100$ G). (*a*) Left polarized parallel waves ($\theta = 0°$); (*b*) left polarized torsional (*solid*) and compressional (*dashed*) oblique waves ($\theta = 45°$).

with the electrons, since the waves are partly right polarized. Beyond $kc/\Omega_p = 100$, the "solid" mode waves can interact with the $^4He^{+2}$ ions and at higher $kc/\Omega_p > 150$ with the protons as well. These interactions produce a deep helium and proton valley when the mode enters the damping ranges, visible in the damping timescale τ_d.

The "dashed" τ_d line starts at low k with a decrease also due to interaction with the electrons, followed by a narrow gap at $kc/\Omega_p \sim 70$ as the mode passes through the heart of the $^4He^{+2}$ resonance region, since the waves available in this region are partially left polarized. Beyond this resonance, "dashed" modes can interact only with the fastest $^4He^{+2}$ ions and with the electrons (the latter with limited efficiency only, since the waves are predominantly not right polarized). This produces a hump of τ_d for $kc/\Omega_p = 80$–130. For $kc/\Omega_p > 130$, these waves undergo heavy damping by thermal protons, which are 10 times as abundant as the $^4He^{+2}$ ions.

The "dotted" branch also starts at low k by a decrease of τ_d due to the interaction with the electrons, since the waves are partly right polarized. At higher $kc/\Omega_p > 50$, interaction with the fastest $^4He^{+2}$ ions produces a shallow depression of τ_d between $kc/\Omega_p \sim 50$ and 90. Above $kc/\Omega_p = 110$, the still partly left "dotted" mode is entering the damping region of the protons, building a deep proton valley.

The case $\theta = 70°$ is represented in Figure 11*c*, for $T = 16 \times 10^6$ K. The "solid" and "dashed" branches of the real part of the dispersion relation have moved visibly downward. The same effect has influenced the "dotted" branch beyond the decoupling point. The bottom panel provides all the already mentioned characteristic damping regions, but their extent and depth have been modified. In particular, the damping is much weaker in the helium and proton cyclotron regions at high k values.

We want to investigate briefly the effect of a more realistic, lower gas temperature. Figure 11*d* represents again the case $\theta = 45°$, but this time for a temperature of 4×10^6 K. Comparing with Figure 11*b* relevant to $T = 16 \times 10^6$ K, the influence of the temperature appears twofold. First, the branches of the dispersion relation move slightly downwards in frequency as T increases. Second, for increasing T, the wave damping by thermal particles becomes stronger (τ_d smaller); in particular, the resonance regions broaden as the thermal velocities rise.

We summarize now the phenomena that appear when we go over from the special case $\theta = 0$ to the general case $\theta \neq 0$. The dispersion relation (real part) then suffers the following changes (compare Fig. 11*a* with Figs. 11*b* and 11*c*, top):

1. The "dashed" and "dotted" branches decouple (see Appendix C).
2. All branches move down slightly to lower frequencies.
3. The polarization changes along each branch, with the appearance of mixed polarizations (see Appendix C).
4. Interaction via higher harmonics, $n \neq \pm 1$, and especially via the $n = 0$ resonance with electrons and protons, becomes possible.

The resulting effects on wave damping can be summarized as follows (Figs. 11*a*–11*c*, bottom):

1. As θ increases, the damping ranges become narrower (see the cos θ dependence of the resonance condition [5]), so that the helium and proton valleys encountered by the "solid" and "dashed" branches narrow down. As a result, the damping timescales at larger k values increase with increasing θ, a major effect for larger values of θ.
2. Wave damping by ions and protons increases wherever the left component increases along a branch and decreases for increasing right component, while for electrons the opposite is true.
3. For increasing θ, the lower k secondary resonance gaps of τ_d of the "dashed" and "dotted" branches, in which the modes cross the helium and the proton valleys, are deepening as well as narrowing down, because of the increasing left-polarized part of the waves in these regions.
4. For increasing θ, the effect of the $n = 0$ resonance with electrons increases, damping any significant right component of the waves, down to low values of k. (But this has no effect on the wave interaction with ions.)

3.2. *Higher Order Resonances*

The resonances with $n \neq 0, 1$ become important when the waves propagate nearly perpendicular to the magnetic field direction, since their influence increases with propagation angle θ (eqs. [7]–[12]). For nearly perpendicular propagation, thermal ions can interact with waves over a large number of extremely narrow resonances scattered over the entire (ω-k) plane. Hence, a complete analysis of the acceleration becomes exceedingly complicated, since the question of acceleration depends extremely sensitively on the temperature and especially on the magnetic field intensity. Such an analysis would exceed by far the scope of this paper. Therefore, we will restrict our present treatment to moderate angles not too close to 90°, where higher order interactions do not contribute significantly to the ion acceleration. This can be shown, e.g., by calculating the contributions of the elements of the dielectric tensor, equations (7)–(12), for small propagation angle in the cases $n = 1$ and $n \gg 1$, and using equation (6). We emphasize, however, that the case of quasi-perpendicular propagating waves is not unimportant. Such waves might play a dominant role in the explanation of the huge enhancements of the ^3He isotope (see, e.g., MVRa for the case of a beam-induced turbulence generation and the special case of the $n = 1$ resonance), and we will analyze this more complicated case in a future paper.

3.3. *The Limits of the Helium Valley, and Their Time Evolution*

The results of § 3.1 allow us to determine the limits of the region, in which preferential gyroresonant $n = 1$ acceleration of heavier ions is impossible due to the strong wave damping by thermal $^4He^{+2}$. Given a wave propagation angle θ and a temperature T, we can find from Figure 11 the frequency ω_l along the dispersion relation, above which the *e*-folding damping time τ_d near the $^4He^{+2}$ gyrofrequency is shorter than a given time interval Δt. For frequencies $\omega > \omega_l$, the waves have suffered substantial damping over the time Δt. Starting with parallel waves $\theta = 0°$, we show in Figure 12*a* the limiting frequency ω_l of the He valley as a function of temperature T, for three different values of Δt. For $\theta = 0°$, only left-polarized Alfvén and $^4He^{+2}$ cyclotron waves will interact with ions in the frequency range close to $\omega/\Omega_p = 0.5$. As expected, the He valley broadens with increasing time and temperature.

For oblique waves, the situation close to $\omega/\Omega_p = 0.5$ becomes more complicated (Fig. 12*b*). If the waves propa-

gate at an angle of $\sim 45°$ with respect to the magnetic field, close to $\omega/\Omega_p = 0.5$ most of the ions will interact with so-called torsional Alfvén waves, which are the equivalent to ordinary left-polarized Alfvén waves in the parallel case (Fig. 11*b*, solid mode). Since these waves twist the magnetic field lines relative to one another, they are also called shear Alfvén waves, or slow Alfvén waves due to their low group velocity $v_A \cos \theta$, where v_A is the Alfvén speed (see, e.g., Swanson 1989, p. 53). Both the $\cos \theta$ dependence in the gyroresonance condition equation (5) and the partial change to linear polarization, however, decrease the extent of the He valley, thus moving the limiting ω_l (*solid lines*) to slightly higher frequencies. The right-polarized Alfvén waves change, for increasing θ, to elliptical polarization (Fig. 11*b*, *dashed mode*). Hence, another secondary He valley appears for these so-called compressional Alfvén waves, where thermal $^4He^{+2}$ ions can interact with their left component. The term "compressional" refers to the compression of the magnetic field lines by the waves. Since this wave type has a larger group speed than the torsional Alfvén waves in the oblique case $\theta \neq 0$, it is also called the fast Alfvén mode. The dashed lines in Figure 12*b* represent the limits of this narrower He valley.

4. RESULTS FOR PREFERENTIAL ACCELERATION OF IONS IN IMPULSIVE SOLAR FLARES

4.1. *Source Plasma Temperatures and Acceleration Timescales*

Based on broad consistency arguments, it had been shown by RMvR that, in impulsive particle events, heavy elements up to Si are accelerated out of gases with temperatures between ~ 2.5 and $\sim 5 \times 10^6$ K, while Fe might possibly be accelerated out of hotter gases up to $\sim 10 \times 10^6$ K as well (see § 1). In this section, we elaborate on these earlier conclusions and tighten these constraints, based now on physical arguments on the damping of waves with $\theta \gtrsim 90°$ in the He valley, and on its change with temperature. So, these tighter constraints will be relevant, provided that the particle acceleration is actually due to non–quasi-perpendicular waves.

To address the question of which elements can be preferentially accelerated, we have to place the gyrofrequencies of their relevant ions relative to the He valley (Figs. 3 and 12). This requires additional information about the fractional abundance f of each charge state in the gas at a given temperature. We show in Figures 13, 14, and 15 the temperature dependence of the ion fraction f for all important charge states of elements C, N, O, Ne, Mg, Si, and Fe, each of these ions being characterized by its value of $\Omega_i/\Omega_p = Q_i/A_i$ for the dominant isotope (Appendix B; see Fig. 14 of RMvR). As an example of the extent of the region of suppressed preferential acceleration due to wave damping, the limit of the He valley versus temperature has been plotted as a vertical wall, for parallel waves at $\theta = 0°$ and $\Delta t = 10^{-3}$ s ($n_e = 10^{10}$ cm^{-3} and $B = 100$ G throughout this section). We cut the temperature distributions of each charge state at the limit of the valley. At any particular temperature, we can then identify, for each element, the approximate fraction of its ions lying outside the He valley, as well as the charge state composition of its preferentially accelerated ions. To improve readability, we omit specifying the isotopic mass in this section, which deals only with the dominant isotope of each element.

Certainly, the sharp cutoff at the limit of the He valley describes only roughly the transition from preferential acceleration outside, to acceleration within the valley that presumably reproduces the coronal abundances relative to ^{4}He. The exact efficiency of preferential acceleration can be obtained only if the wave generation process is specified, and by calculating the Fokker-Planck coefficients for interaction between the different ions and the relevant plasma modes. For oblique waves, these coefficients are extremely complicated, and a detailed calculation would definitely exceed the scope of this paper (see Jaekel & Schlickeiser 1992; Schlickeiser 1995). Moreover, it would require the inclusion of more approximations and assumptions about the detailed features of the turbulence, diluting the clear idea of the He valley. For our purpose of determining the constraints on any gyroresonant model with $\theta \gtrsim 90°$ waves, imposed by the mere existence of the He valley and the composition observations, an investigation of the detailed efficiency and the influence of the injected wave spectrum is not necessary; we will address this question in a future paper.

Figure 13 shows that all charge states of Fe between $Q = +12$ and $+22$ can be preferentially accelerated, extending from low temperatures and gyrofrequencies around 0.25 Ω_p to $T \sim 15 \times 10^6$ K and frequencies around 0.40 Ω_p. Only charge states $Q \gtrsim +22$ lie inside the He valley and cannot be preferentially accelerated. Various Fe ions might thus be preferentially accelerated out of any AR or flare gas with temperature up to $\sim 15 \times 10^6$ K (for $\theta = 0°$ and $\Delta t = 10^{-3}$ s).

In order to visualize better the regions of preferential acceleration of the other enhanced elements Ne, Mg, and Si, we have magnified in Figure 14 the low-temperature–high-frequency region relevant to these elements. Here the He valley prevents preferential acceleration of Si^{+12} above $\sim 3.2 \times 10^6$ K, and of Mg^{+10} above $\sim 5.5 \times 10^6$ K. At this latter temperature, for instance, only $\sim 10\%$ of all Ne is still in the form of Ne^{+8}, and the dominant higher charge states

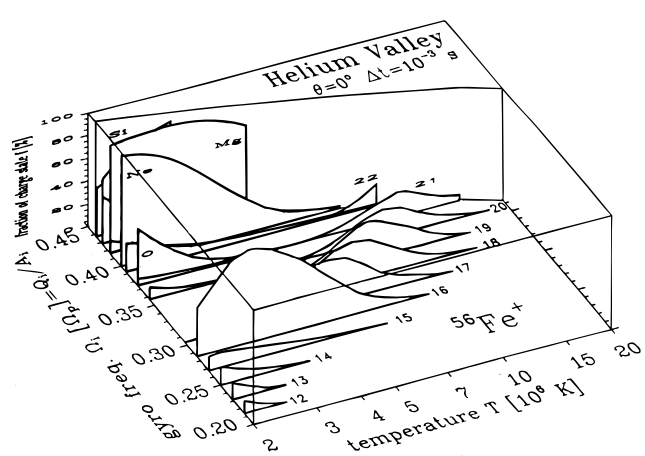

FIG. 13.—Charge states outside the helium valley. The fractional abundance of each charge state of the principal elements is plotted vertically as a function of temperature. Each charge state is represented on the frequency scale at its own value of $\Omega_i/\Omega_p = Q_i/A_i$ for the dominant isotope. The charge state fractions are plotted only when they lie outside the He valley for $\theta = 0°$ and $\Delta t = 10^{-3}$ s, which is represented schematically by a vertical wall ($n_e = 10^{10}$ cm^{-3}, $B = 100$ G).

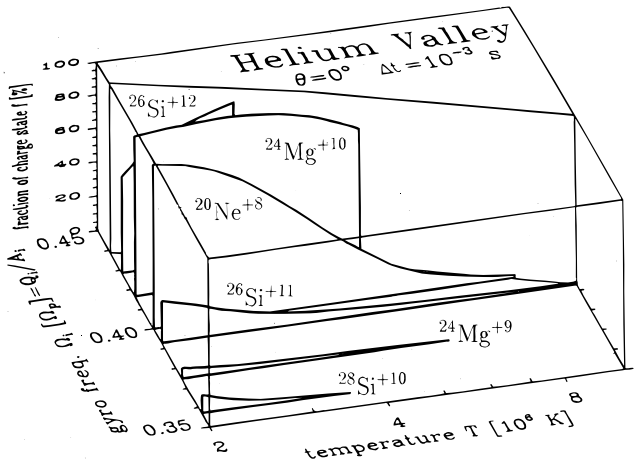

FIG. 14.—Blowup of Fig. 13, showing only the ions of Ne, Mg, and Si

$Ne^{+9,+10}$ are located within the He valley. Therefore, the observed approximately equal enhancements of Ne, Mg, and Si (RMvR), together with the extent of the He valley, require the selection to take place in the low-temperature region below $\sim 3.2 \times 10^6$ K, where (i) Ne^{+8} makes up, say, $>50\%$ of Ne, and (ii) dominant Si^{+12} still lies outside the valley (for $\theta = 0°$ and $\Delta t = 10^{-3}$ s).

The observational fact that C, N, and O are in general not enhanced relative to each other and to $^4He^{+2}$ (RMvR) yields another limit for the acceptable temperature range. In Figure 15, the significant charge states of these light elements are plotted in another magnified picture of the region close to the He valley. Obviously, C^{+5} never exceeds 10% of C, and dominant C^{+6} with $Q/A = 0.5$ lies deep in the valley, so that C should not be enhanced relative to $^4He^{+2}$, for all relevant temperatures. But the dominant O^{+7} is preferentially accelerated below $T \sim 2.1 \times 10^6$ K, and preferentially accelerated $N^{+5,+6}$ and O^{+6} become significant at low temperatures, exceeding, say, 20% of the elemental abundances below 2.6×10^6 K. So, the selection should generally take place above $\sim 2.6 \times 10^6$ K (for $\theta = 0°$ and $\Delta t = 10^{-3}$ s).

To quantify these two limits for the range of agreement with the observations, we have calculated, for each element, the total fraction F of all ions lying outside the He valley,

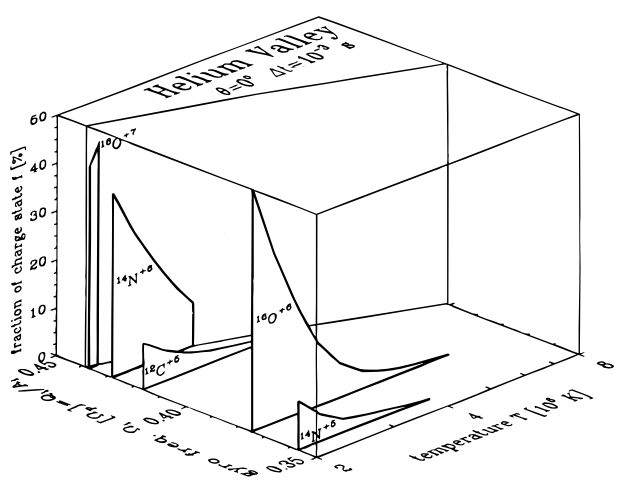

FIG. 15.—Blowup of Fig. 13, showing only the ions of C, N, and O

for all considered values of θ, Δt, and T. The fraction F can be obtained by projecting, in Figures 13, 14, or 15, the sum of all charge states of an element lying outside the He valley, onto the vertical f-T plane. In Figure 16, F is plotted as a function of temperature for C, N, O, Ne, Mg, Si, and Fe. A smooth temperature variation of F reflects the smooth temperature variation of the ionic fraction of a charge state that lies outside the valley, while a sharp step reflects a specific charge state entering the valley at a specific temperature (this sharp jump is, of course, an oversimplification). We have chosen two examples, $\theta < 20°$, $\Delta t = 10^{-2}$ s and $\theta = 45°$, $\Delta t = 10^{-3}$ s, to illustrate the principal results (neglecting interaction with compressional Alfvén waves).

In the case $\theta < 20°$ and $\Delta t = 10^{-2}$ s (Fig. 16*a*), the valley is very broad. The equal enhancements of Ne, Mg, and Si require $T < 2.1 \times 10^6$ K, in order to have the predominant Si^{+12} lie outside the He valley. On the other hand, the condition that the fractions of N and O outside the valley be small, say, $<20\%$, requires $T > 2.5 \times 10^6$ K; at lower temperatures, indeed, the fraction of He-like O^{+6}, lying far outside the valley, exceeds $\sim 20\%$ (predominant H-like O^{+7} always lies within the valley). For this parameter range, therefore, no agreement with the observations can be obtained: at the temperatures at which O is not enhanced, most of the Si lies within the He valley.

In the case $\theta = 45°$ and $\Delta t = 10^{-3}$ s (Fig. 16*b*), the valley is narrower. Predominant H-like O^{+7} now lies outside the valley up to temperatures as high as $T = 2.6 \times 10^6$ K. But predominant Si^{+12} lies outside the valley up to 4×10^6 K. Further, Ne^{+8}, lying far outside the valley, makes up the major fraction of Ne up to $T \sim 3.8 \times 10^6$ K. Preferential acceleration of Mg obviously imposes no additional constraints. In this case, therefore, we find that an agreement with the observations is possible over a significant range of temperatures, between ~ 2.6 and $\sim 3.8 \times 10^6$ K. These limits, of course, depend on the efficiency of the acceleration process outside the valley and are only approximate values.

To sum up, we present in Figure 17 the range of agreement with observed compositions as a function of Δt and T, for $\theta < 20°$ and $\theta = 45°$. We consider that the lack of enhancement of O relative to C requires that the fraction F of ions lying outside the valley be $<20\%$ for O. This condition determines the lower acceptable temperatures. For large Δt values, only O^{+6} lies outside the valley, making up $<20\%$ of O above $T \sim 2.6 \times 10^6$ K. For smaller Δt values, even dominant O^{+7} tends to lie outside the valley; the smaller the Δt, the higher the temperature required to have the valley include it. To account for the nearly equal enhancements of Ne, Mg, and Si, we require that the fraction F be $>50\%$ for these three elements. This condition determines the higher acceptable temperatures. Ne^{+8}, always lying outside the valley, makes up $>50\%$ of Ne only below $T \sim 3.8 \times 10^6$ K. As for Si^{+12}, the larger the Δt, the lower the maximal temperature acceptable to prevent the valley from including it. Mg does not place any additional constraint on the acceptable range of T and Δt for elements up to Si.

In general we find that, as suggested by Figure 17 for waves with $\theta \leq 45°$, acceleration after $\Delta t > 5 \times 10^{-3}$ s will be impeded by the He valley, making an enhancement of Si without enhancement of O impossible, in contradiction with the observations (see Fig. 16*a*). At the other extreme, preferential acceleration within $\Delta t < 10^{-4}$ s will not be hindered by the He valley, making an enhancement of Ne

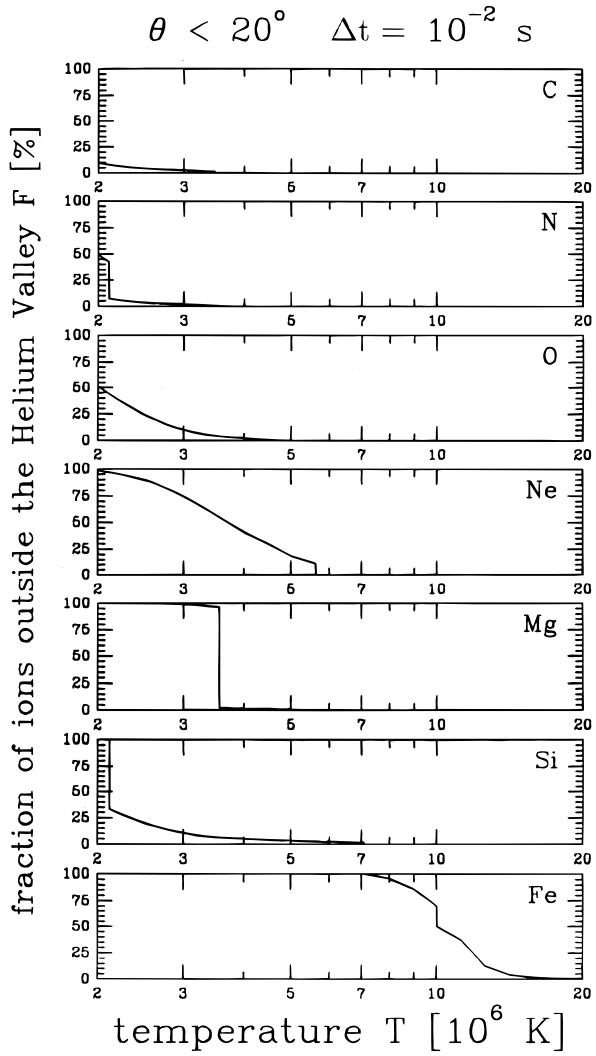

FIG. 16*a*

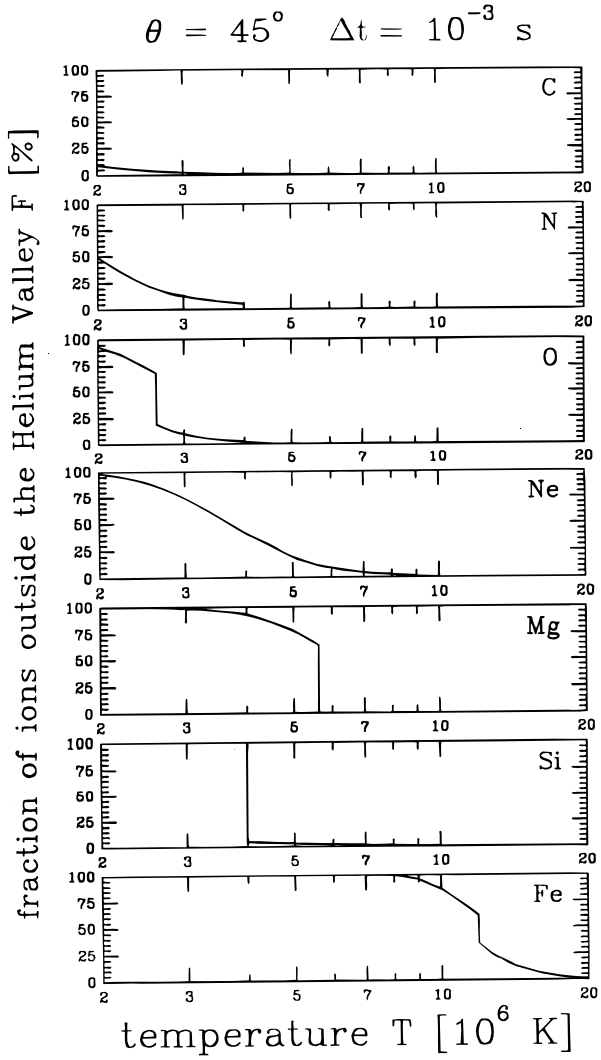

FIG. 16*b*

FIG. 16.—The total fraction F of all ions of each element that lie outside the helium valley, as a function of temperature for two situations: (*a*) a very broad He valley for $\theta < 20°$, $\Delta t = 10^{-2}$ s, and (*b*) a narrower He valley for $\theta = 45°$, $\Delta t = 10^{-3}$ s ($n_e = 10^{10}$ cm^{-3}, $B = 100$ G). Each sharp step with temperature is the schematic representation of one particular charge state entering the He valley when $\tau_d = \Delta t$, due to the broadening of the valley with increasing temperature.

without enhancement of O impossible, again in contradiction with the observations (see Fig. 16*b*, without suppression of O^{+7} beyond 2.6×10^6 K). Therefore, we conclude that for roughly parallel waves ($\theta \leq 45°$), the existence of the He valley, and its broadening as time passes, implies that only source plasma temperatures around ~ 2.6 to $\sim 3.8 \times 10^6$ K and timescales for preferential acceleration $\sim 10^{-4}$ to $\sim 5 \times 10^{-3}$ s are consistent with the observed abundances of elements up to Si (for the Arnaud & Rothenflug [1985] nominal ionization equilibrium and our nominal values of $n_e = 10^{10}$ cm^{-3} and $B = 100$ G).

Observations by Mason et al. (1986, 1994) have, however, suggested that, in a small fraction of the events, O is moderately enhanced relative to C (§ 1). If this is, indeed, the case, the lower limit to our acceptable temperature ranges are somewhat relaxed in these particular events (as well as the associated limits for Δt).

We ask now the following question: Does the preferential acceleration process have to take place exclusively in gases below $\sim 3.8 \times 10^6$ K? Or, could it continue (e.g., for Fe) in hotter gases as well, in which all elements up to Si would just be totally excluded from the acceleration because all their ions lie within the He valley? This latter hypothesis can probably be rejected. As shown in Figure 17, for larger Δt values within the allowed range, the Si/Ne ratio limits severely the acceptable gas temperatures to values $< 3.8 \times 10^6$ K. For the smaller Δt values that allow acceleration up to 3.8×10^6 K, Mg continues to lie outside the He valley up to some ~ 5 or $\sim 6 \times 10^6$ K. If acceleration proceeded significantly in gases at temperatures between ~ 3.8 and $\sim 6 \times 10^6$ K, no Ne, possibly no Si, but certainly significant amounts of Mg would be accelerated there. This would produce specific enhancements of at least the Mg/Ne ratio, in contradiction with observation.

Interesting and important is the analysis of Fe, which is always ~ 3 times as enhanced as Ne, Mg, and Si (RMvR). In both cases presented in Figure 16, preferential acceleration of Fe is in principle possible up to $T \sim 12 \times 10^6$ K. It seems, however, most likely that Fe is accelerated together with the Ne, Mg, and Si ions, out of the same gases at $T \sim 3 \times 10^6$ K. The higher enhancement of Fe relative to Ne, Mg, and Si can then easily be due to a higher efficiency

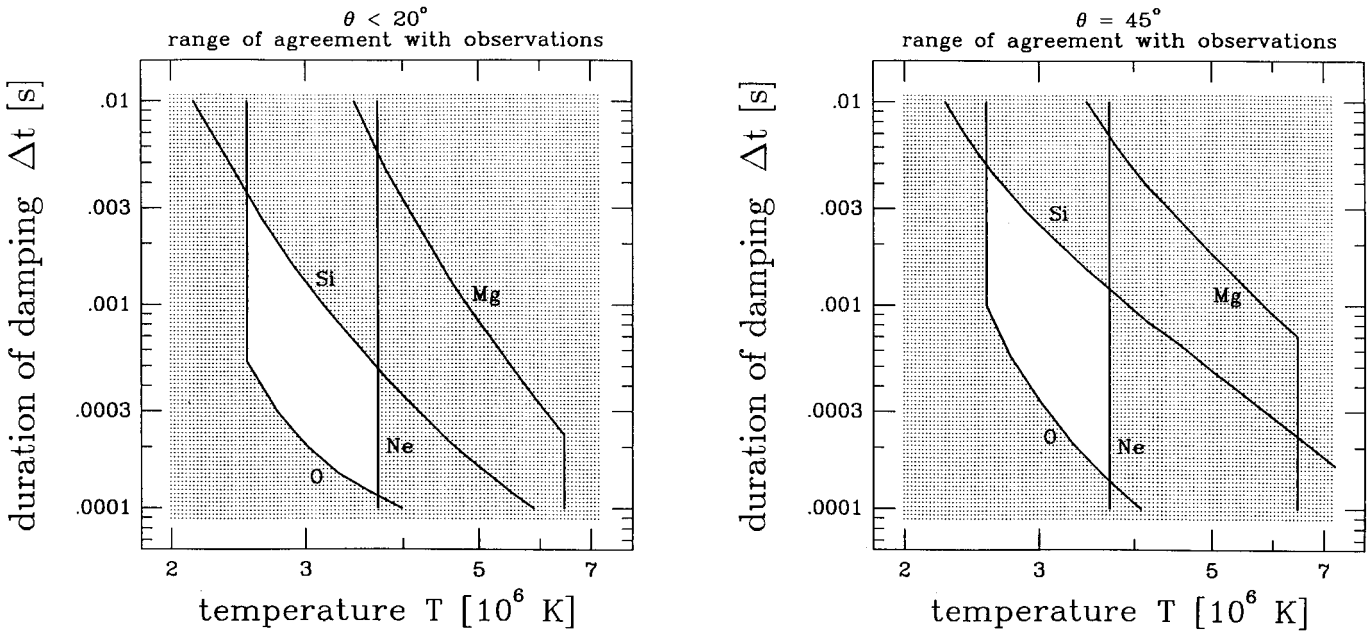

FIG. 17*a* FIG. 17*b*

FIG. 17.—The white range indicates the approximate range of agreement with the observed accelerated particle composition, as a function of the source plasma temperature and of the timescale Δt for preferential ion acceleration. The two cases $\theta < 20°$ and $\theta = 45°$ are presented ($n_e = 10^{10}$ cm^{-3}, $B = 100$ G). On the right of the O line, the fraction of O outside the He valley is $<20\%$, as required. On the left of the Ne, Si, and Mg lines, the fraction of these elements outside the valley are $>50\%$, as required.

of acceleration of the lower $Q/A \sim 0.28$ Fe ions, as compared to the Ne, Mg, and Si ions with $Q/A \sim 0.42$ (Fig. 13). The hypothesis of an additional, continued acceleration of the sole Fe (elements up to Si being all close to fully stripped), while the flaring loop is being heated progressively to $>10 \times 10^6$ K, indeed, faces several difficulties: (i) we have just noted that the observed Mg/Ne ratio suggests that little acceleration takes place out of gases in the ~ 4 to $\sim 6 \times 10^6$ K range; (ii) the relative stability of the observed Fe overenhancement relative to Ne, Mg, and Si (RMvR) does not suggest different source media; and (iii) the escape of the observed energetic particles out of the hot flaring loop itself would be problematic.

In any case, such a putative hot component would not solve the problem of the high charge states of the energetic Fe observed by Luhn et al. (1987), which, if thermal in origin, imply very hot source gases, predominantly with $T \gtrsim 10 \times 10^6$ K (see discussion in § 1). It would, indeed, seem unlikely that only very little Fe is accelerated near 3×10^6 K; in addition, even temperatures in the range ~ 3 to $\sim 12 \times 10^6$ K are insufficient to explain the high observed charge states. So, a stripping of the Fe ions after acceleration, possibly by energetic electrons (MV; RMvR), would seem inescapable. One would then expect energetic lighter elements below Si to be fully stripped, which is consistent with the Luhn et al. (1987) scarce observations of the energetic Si charge states.

4.2. *Discussion, Dependence on the Conditions in the Source Plasma, Role of a Possible Wave Cascading*

We have obtained a temperature range from ~ 2.6 to $\sim 3.8 \times 10^6$ K for the source gas of the escaping particles. These limiting temperatures have been derived essentially from the ionization balances between the O^{+6} and O^{+7} ions, and the Ne^{+8} and Ne^{+9} ions, respectively. These ionization balances between He-like and H-like ions are quite reliably calculated (Arnaud & Rothenflug 1985). When conservative uncertainties on the atomic physics parameters are folded in (Arnaud 1995), the above range of possible source gas temperatures is extended to, at the most, ~ 2.4 to $\sim 4.5 \times 10^6$ K.

This temperature range is comparable to that of ordinary AR gases (Appendix A), not of flaring loops. This represents a confirmation and a refinement of the result of RMvR. It implies that the particles are accelerated, either in the AR gas *surrounding* the flaring loop itself, or within the flaring loop *before* it was heated (see § 1).

This temperature range, as well as the timescales obtained for ion acceleration after turbulence injection ($\Delta t \sim 10^{-4}$ to $\sim 5 \times 10^{-3}$ s), were based on our nominal values of $n_e = 10^{10}$ cm^{-3} and $B = 100$ G. Now, the more common (at least quiescent) AR plasma densities and fields show somewhat lower densities $n_e \sim 1$ to $\sim 4 \times 10^9$ cm^{-3} and slightly higher fields $B \sim 50$ to ~ 400 G; they are less overdense, more around the overdense-underdense boundary (Appendix A). It is useful to discuss qualitatively the modification of the above results for such, probably more relevant, plasmas. The acceptable temperature range should not be affected significantly by such changes. The damping, by contrast, would then become less efficient because (i) for unchanged physics of the wave-ion interaction, i.e., for a fixed position of the dispersion relation in the (ω-k) plane, obviously the damping timescale τ_d is $\propto 1/n_e$, and (ii) in addition, the dispersion relation moves toward lower values of k, hence out of the damping range " triangles " in the (ω-k) plane (e.g., Figs. 4 or 11*b*). So the required acceleration timescales Δt may be somewhat larger than those found above, by, say, a factor of ~ 10 or so. This will be studied qualitatively in a forthcoming paper.

Our assumption of an instantaneous injection of the wave energy in the neighborhood of $\Omega_{^4He^{+2}}$ is probably not realistic, due to the steady cascading of large-scale, low-k–

low-ω waves (Miller & Roberts 1995), whose injection may, in addition, be also continuous. Most probably, the He valley will be, to some degree, replenished continuously with waves. The injected wave energy should vary smoothly with ω, i.e., be roughly frequency independent in the neighborhood of $\Omega_{^4He^{+2}}$. By contrast, the rate of wave energy dissipation by interaction with $^4He^{+2}$ ions decreases away from $\omega = \Omega_{^4He^{+2}}$, following the shape of the Maxwell distribution for the differential ion density versus v_z. For a given rate of cascading (not too high), there will therefore exist a frequency $\omega_c < \Omega_{^4He^{+2}}$ at which wave replenishment by cascading just balances wave damping and hence prevents the valley's further broadening. If cascading is very intense, the He valley will thus be limited to the peak of the Maxwell distribution for v_z (or even may not form at all). On the other extreme, without any cascading, the He valley may broaden indefinitely, as the waves with frequencies further and further from $\Omega_{^4He^{+2}}$ progressively become damped by the rarer and rarer $^4He^{+2}$ ions along the Maxwell tail. In this context, our "effective damping duration" Δt can be interpreted as the time it takes, in the instantaneous injection approximation, for the He valley to broaden down to the above frequency ω_c at which cascading just balances damping. Obviously, the higher the steady wave injection rate, the narrower the maximal width of the He valley, and the shorter the equivalent damping during Δt. In this context, the above conclusions on the acceptable Δt values actually set constraints on the acceptable rates of wave cascading.

On the other hand, several effects may, on the contrary, broaden the He valley. They may have to be considered in later studies. Offhand, at least three effects can be imagined:

1. For strong turbulence, waves may interact with particles even if the gyroresonance condition is only approximately fulfilled (§ 2.2). This may broaden the He valley.

2. Suprathermal tails are commonly observed in solar wind distribution functions (see Scudder 1992; Ogilvie et al. 1993), starting at densities of typically 10^{-2} to 10^{-3} times the Maxwellian peak density (Fig. 2). It has been suggested that such tails may exist in the corona as well (Scudder 1992); if they do, they will also broaden the He valley.

3. In this, as in all previous studies, we have not considered possible nonuniformities in the intensity of the magnetic field B. If the waves propagate through a medium with a nonuniform field intensity, the range of frequencies ω over which the waves are damped by resonant interaction with $^4He^{+2}$, with gyrofrequency $\Omega_{^4He^{+2}} \propto B$, i.e., the He valley, will be effectively broadened. An effective broadening of the valley by $\sim 2\%$ of $\Omega_{^4He^{+2}}$ would alter significantly the heavy element composition (see Figs. 12 and 17 for $T \sim 3 \times 10^6$ K). The relevant He cyclotron waves near the boundary of the He valley travel at speeds roughly on the order of $\sim \frac{1}{3}$ of the Alfvén speed (Fig. 10*b*). For the Alfvén speed $v_A = 2 \times 10^3$ km s^{-1} resulting from our nominal $n_e = 10^{10}$ cm^{-3}, $B = 100$ G, and an associated typical wave lifetime of $\sim 7 \times 10^{-4}$ s (Fig. 17), field inhomogeneities of $\sim 2\%$ over scales of ~ 0.5 km would change significantly the heavy element composition. For more typical quiescent AR conditions, i.e., $n_e \sim 2 \times 10^9$ cm^{-3}, $B \sim 200$ G, yielding Alfvén speeds $v_A \sim 10^4$ km s^{-1} (Appendix A) and, say, 10 times larger acceleration times, the same $\sim 2\%$ field inhomogeneities over scales of ~ 20 km would suffice to alter significantly the composition of the accelerated heavy elements. Of course, this constraint becomes even more severe if the acceleration lasts longer, Δt representing the timescale for saturation of the width of the He valley due to cascading.

Regarding energetics, the He valley can, of course, exist only if wave damping by $^4He^{+2}$ isotopes is, indeed, severe, i.e., if the wave energy injected near the $^4He^{+2}$ gyrofrequency is *not* sufficient to kick *all* the $^4He^{+2}$ isotopes in the gas off the thermal distribution. This condition is certainly met, were it only because the depletion of the accelerated NeMgSi *relative to Fe* indicates that, even for these much rarer species, *not all* ions in the gas are being accelerated.

Turning to the other extreme case, that of comparatively small injected wave energies, one may consider the possibility of a significant wave damping, not only by ^4He isotopes, but also by the rarer heavy ions themselves (if wave cascading is important, damping by Fe at low k, low ω will then act as a first wave filter). Qualitatively, the enhancement of each individual ion outside the He valley would then be larger, if its own source gas abundance is smaller (provided that its gyrofrequency $\Omega_i \propto Q_i/A_i$ is sufficiently separated from those of neighboring ions). In this context, the observed extra enhancements of the ~ 10- to ~ 20-fold rarer Na, Al, ^{22}Ne, and $^{25,26}Mg$, as compared to the neighboring dominant species ^{20}Ne, ^{24}Mg, and ^{28}Si (Reames 1993, 1995; Mason et al. 1994), might possibly indicate that wave damping by ^{20}Ne, ^{24}Mg, and ^{28}Si (with coronal abundances ~ 300 times lower than ^4He) is significant.

We recall also that, although underdense plasma conditions have not been investigated explicitly here, preliminary calculations have shown that the present model for selective ion acceleration applies also for an underdense plasmas, as long as quasi-perpendicular waves do not dominate over moderately oblique waves.

5. SUMMARY

We have studied in detail the behavior (i.e., the dispersion relation and damping) of parallel plasma waves in hot plasmas as a function of the temperature, in the presence of all the major and minor ions actually present in coronal plasmas. The key role played by abundant $^4He^{+2}$ in wave damping is stressed ("helium valley" of strong wave damping). This allows us to consider a simpler *e*-*p*-$^4He^{+2}$ plasma to generalize our study to oblique waves and investigate their dispersion relation, polarization, and damping. Damping via higher order resonances can be neglected, except for quasi-perpendicular waves. The larger the wave angle to the field, the narrower the frequency range of the wave damping by $^4He^{+2}$ ions.

We have then interpreted the elemental composition anomalies among the ions accelerated during impulsive solar energetic particle events, in terms of the damping of the waves available for their acceleration. The damping of all moderately oblique waves by $^4He^{+2}$ ions, preventing any preferential acceleration of ions with charge-to-mass ratio Q/A close to 0.5, can, indeed, shape the heavy element composition of the accelerated particles. The hotter the plasma, the wider the range of Q/A values for which ions are excluded from preferential acceleration. In this context, we have shown that the observed composition requires the following:

1. The source gases of all accelerated heavy ions must have predominantly temperatures between ~ 2.4 and $\sim 4.5 \times 10^6$ K, roughly comparable to ordinary (quiescent,

and probably flaring) active region (AR) gas temperatures. This result points to the AR gas in which the flare develops as the source of the energetic ions. The acceleration must take place, either prior to the flare heating, or predominantly in the AR gas surrounding the hot flare itself. This result refines the earlier one of RMvR, on the basis of a more specific analysis.

2. As a result, the elemental composition of the impulsive event energetic particles can be understood, provided that the denser parts of ARs indeed have predominantly temperatures above $\sim 2.4 \times 10^6$ K, as very often, but not always, observed; it would be difficult to understand if the bulk gas in (flaring) ARs were largely cooler than $\sim 2.4 \times 10^6$ K (Appendix A).

3. The high energetic Fe and Si charge states observed by Luhn et al. (1987) require confirmation. If confirmed, they require stripping after the ions have been extracted from the thermal pool, possibly by energetic electron beams.

4. The acceleration timescale or, in case of the presence of wave cascading, the time over which the growth of the He valley is not hindered by wave cascading (§ 4.2), must lie somewhere between $\sim 5 \times 10^{-4}$ and $\sim 3 \times 10^{-2}$ s, for our nominal plasma density and magnetic field strength of $n_e = 10^{10}$ cm^{-3} and $B = 100$ G. This timescale could be larger, by a factor of, say, ~ 10, if the typical conditions in quiescent ARs ($n_e \sim 1$ to $\sim 4 \times 10^9$ cm^{-3}; $B \sim 50$ to ~ 400 G) also apply to the bulk $\sim 3 \times 10^6$ K gas of those ARs in which a flare takes place and accelerates particles (as possibly suggested by the source gas temperature we obtained).

For such quiescent AR conditions, the plasmas lie in the neighborhood of the overdense-underdense boundary; both slightly underdense and slightly overdense situations are probably common. The above conclusions are valid irrespective of whether the source plasma is overdense or underdense, provided that quasi-perpendicular waves (possibly generated by electron beams) do not dominate over moderately oblique waves (possibly generated by wave cascading) in the source plasma of the accelerated particles.

This work has been initiated, and its essential points laid down, while J. S., J. P. M. and A. S. were at the Laboratory for High Energy Astrophysics at NASA/Goddard Space Flight Center. We thank Jim Miller, Reuven Ramaty, and Reinhard Schlickeiser for helpful discussions, and Jim Miller for making his plasma dispersion function code available to us. Discussions with Nancy Brickhouse, Jeff Brosius, Julia Saba, Joan Schmelz, Keith Strong, and Ken Widing have been essential for assessing the physical conditions in active region plasmas. The expertise of Monique Arnaud, Jacques Dubau, and Takako Kato has been precious in helping us evaluate the uncertainties on the ionization balances. We benefited from discussions with Joe Mazur on the charge state measurements. We also wish to thank the anonymous referee for his thorough review, which helped us improve this paper. J. S. acknowledges support from NASA SR&T grant 665-170-38-53-09 and the Alexander von Humboldt-Stiftung. J. P. M. acknowledges receipt of a National Research Council-GSFC Senior Research Associateship. A. S. thanks Reuven Ramaty for the opportunity to work at GSFC and for his kind hospitality.

APPENDIX A

ACTIVE REGION TEMPERATURES, DENSITIES, AND MAGNETIC FIELDS

The temperature of ~ 2.4 to $\sim 4.5 \times 10^6$ K obtained for the source gas of the escaping accelerated particles (§§ 1 and 4), warmer than quiet coronal temperatures, but much cooler than usual flaring gas temperatures, is to be compared with active region (AR) temperatures.

Recent studies generally give evidence for a central region of denser, warmer gas, sometimes found remarkably isothermal, surrounded by more dilute, cooler gases. Many studies yield denser material temperatures quite closer to $\sim 3 \times 10^6$ K or slightly above (Pye et al. 1978; Saba & Strong 1991a, 1991b; Nitta et al. 1991; Brosius et al. 1982, 1996; Schmelz et al. 1994; Schmelz 1995; Yoshida & Tsuneta 1996); others may be consistent with predominant temperatures anywhere between ~ 2.5 and $\sim 3 \times 10^6$ K (Hara et al. 1992; Waljeski et al. 1994; Brickhouse, Raymond, & Smith 1995; see also Klimchuk & Gary 1995), and others show temperatures lying more definitely around $\sim 2.5 \times 10^6$ K (Brosius et al. 1992, 1993, 1994). In some cases, large clumps of cooler material around ~ 1.5 to $\sim 2 \times 10^6$ K are also being found (Schmelz et al. 1992, 1994; Brosius et al. 1996). A minor amount of hotter (e.g., $\sim 5 \times 10^6$ K) gas is sometimes present, possibly related to some low level of flaring activity (Saba & Strong 1991b; Hara et al. 1992; Brosius et al. 1996; Yoshida & Tsuneta 1996).

Brickhouse et al. (1995) have performed a particularly elaborate study of AR temperatures, based on a broad range of ionization states from Fe^{+8} ($\sim 0.5 \times 10^6$ K) to Fe^{+16} ($\sim 5 \times 10^6$ K), on a large number of lines, and on reevaluated emissivities. Rather than a single "best" temperature, they derive a full temperature distribution for gas, which is dominated by a well-defined peak with HWHM $\sim 1 \times 10^6$ K, centered at 2.5×10^6 K if Arnaud & Rothenflug's (1985) ionization balance is adopted, and at 3.4×10^6 K if Arnaud & Raymond's (1992) balance is adopted instead (different dielectronic recombination rates). Brickhouse et al. find only a weak lower temperature tail in the emission measure distribution down to 0.5×10^6 K. A similar study has been performed recently by Brosius et al. (1996), with a similar outcome for one AR, and a broad temperature range for another one.

From the theoretical point of view, the radiative loss function shows a minimum right between ~ 3.0 and $\sim 4.0 \times 10^6$ K, with a steep rise up to a rough plateau located below $\sim 1.0 \times 10^6$ K (Cook et al. 1989). So gases with temperatures between ~ 3.0 and $\sim 1.0 \times 10^6$ K should be temperature instable. This might explain a possible clustering of AR temperatures not far from 3×10^6 K and a scarcity of cooler material.

Many of the above studies further yield typical AR densities of $n_e \sim 1$ to $\sim 4 \times 10^9$ cm^{-3}, and fields of $B \sim 50$ to ~ 400 G (Pye et al. 1978; Nitta et al. 1991; Brosius et al. 1992, 1993; Schmelz et al. 1992, 1994; Cook et al. 1994; Brickhouse et al. 1995). While the accuracy of these determinations is limited (e.g., filling factors), we will take them as indicative. With such values,

the plasma frequency–to–electron gyrofrequency ratio ω_p/Ω_e lies typically in the ~ 0.25 to ~ 4 range, so that the plasma lies in the neighborhood of the underdense-overdense limit n_e [cm^{-3}] $\approx 10^5 \times B^2$ [G]. It is therefore likely that both slightly overdense and slightly underdense situations occur in practice. These values also yield typical Alfvén speeds of $v_A \sim 10^4$ km s^{-1}.

An additional caveat is required: most of the above studies pertain to quiescent ARs. The scarce specific data do not suggest that physical conditions in the bulk gas of those ARs within which a flare takes place (outside the flare itself) are very different from those of quiescent ARs (Brickhouse et al. 1995; Saba 1995; Brosius 1995). There is, however, evidence for the presence of some hotter gas an hour or so prior to and after some flares (Saba & Strong 1991b; Saba 1995). In brief, while there is no indication of large differences, there is no guarantee that the conditions in those ARs within which a flare takes place are exactly the same as in quiescent ARs.

Clearly, our strict conclusion that the source gas of the energetic particles includes very little material below 2.4×10^6 K is easy to understand if the denser parts of (flaring) ARs usually have temperatures close to 3×10^6 K or slightly above, but it poses a serious problem if these temperatures lie commonly around 2.5×10^6 K only.

APPENDIX B

ABUNDANCES OF IONS IN THE SOURCE CORONAL PLASMA

Here we summarize the ion abundances in the source plasma adopted throughout this paper. The particles accelerated in impulsive events have, in all likelihood, been extracted out of active region (AR) coronal gas. It has been confirmed by RMvR that the elemental composition of the energetic particle parent gas is indeed, to first order, of "coronal," rather than photospheric, type. For this "coronal" composition, we adopt the accurate composition of gradual-event solar energetic particles (gradual-SEP), which should be representative of the slow solar wind and of its source gas in the large scale corona outside coronal holes (e.g., Meyer 1993a, 1993b, 1996a, 1996b). It goes as follows: H = 730,000, He = 36,500, C = 269, N = 77, O = 621, Ne = 88, Mg = 121, Si ≡ 100, Fe = 97 (with errors <20%, except possibly for H and He). These values have been derived from the gradual-SEP observations of Breneman & Stone (1985) and reinterpreted on the basis of the meteoritic determination of the photospheric Fe abundance (e.g., Grevesse & Noels 1993); they agree well with other, equivalent determinations (Meyer 1985a; Garrard & Stone 1993; Reames 1995).

The composition of the coronal gas within ARs, which is directly relevant here, could differ from this adopted composition of the slow solar wind gas, which might originate in specific, narrow, open-field channels squeezed between coronal loops (e.g., Wang, Sheeley, & Nash 1990; Wang 1994; Sheeley 1995; Meyer 1993a, 1993b, 1996a, 1996b). Actually, the large body of extreme-ultraviolet (EUV) and X-ray observations of major elements within well-developed ARs in most cases yield compositions quite similar to the above adopted ones (e.g., Meyer 1993a, 1993b, 1996a, 1996b). There are, however, also signs for deviations. The current γ-ray line data analysis suggests systematically ~ 1.7 times larger Ne/O ratios in low-altitude flare material (Ramaty et al. 1995). Occasionally, X-ray observations also yield ~ 2.5 times higher Ne/O ratios in AR gases (see Meyer 1993a, 1993b, 1996a, 1996b). Such excesses could possibly be related to the observed ~ 1.5 times excess of Ne relative to Mg and Si in the impulsive event energetic particles, as compared to the gradual-SEP composition (RMvR). Several EUV and X-ray studies have also found significant excesses of rarer, very low FIP elements with FIP $\lesssim 6$ eV in coronal gases, as compared to gradual-SEP's (see Meyer 1996a, 1996b).

The adopted isotopic ratios are those of Anders & Grevesse (1989), which are probably valid for the entire solar environment.

The ionic fraction f of each charge state of the various elements at a given temperature, assumed at equilibrium, were taken from Arnaud & Rothenflug (1985). For consistency with the other elements, we preferred not to use the Arnaud & Raymond (1992) assessment for Fe, but its use would not change anything in our conclusions.

APPENDIX C

DISCUSSION OF THE WAVE POLARIZATION IN A COLD ELECTRON-PROTON-HELIUM PLASMA

The change of polarization of the waves with increasing propagation angle θ is of crucial importance for the understanding of the complex damping landscape in a hot solar plasma. In this Appendix, we review briefly the major effects, which are used extensively throughout the paper, in the simpler case of a cold electron-proton-helium plasma. While the formulae can be found in the literature, we are not aware of any detailed analysis of the resulting polarization features, even for a cold electron-proton-helium plasma.

The polarization vectors $\boldsymbol{e}^{\pm}$ of the two wave modes in a cold electron-proton-helium plasma can be written as (see, e.g., Melrose 1986, p. 53)

$$\boldsymbol{e}^{\pm} = \frac{K_{\pm}\boldsymbol{\kappa} + T_{\pm}\boldsymbol{t} + i\boldsymbol{a}}{(K_{\pm}^2 + T_{\pm}^2 + 1)^{1/2}},$$

with

$$T_{\pm} = \frac{DP\cos\theta}{An_{\pm}^2 - PS}, \qquad K_{\pm} = \frac{(P - n_{\pm}^2)D\sin\theta}{An_{\pm}^2 - PS},$$

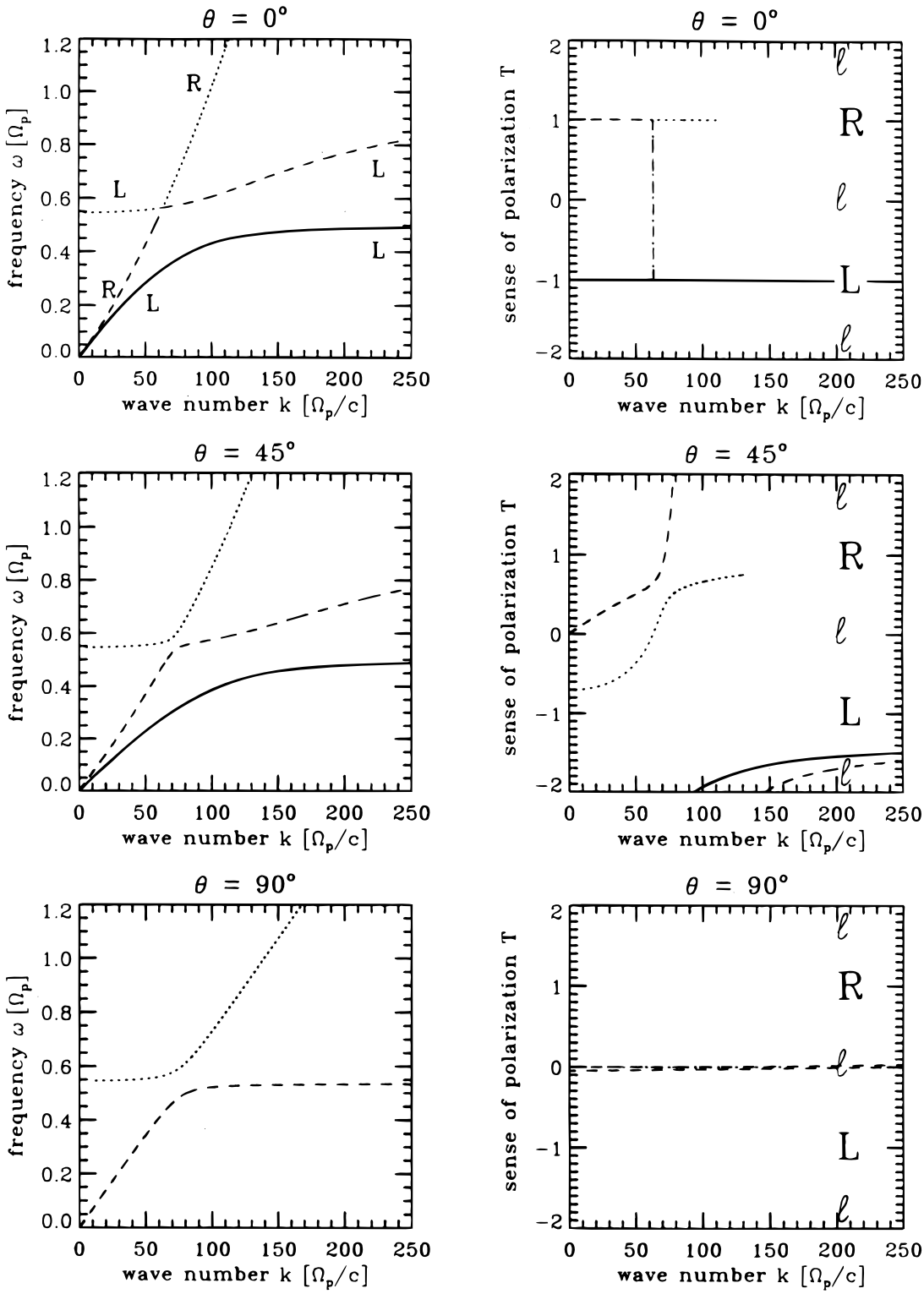

FIG. 18.—Dispersion relation (*left*) and sense of polarization T (*right*) as a function of wavenumber k in a cold *e-p*-He plasma, for propagation angles $\theta = 0°$ (*top*), 45° (*middle*), and 90° (*bottom*). The three branches of the dispersion relation, and their corresponding polarizations, are plotted as solid, dashed, and dotted lines. $T > 0$ and $T < 0$ indicate right and left polarization, respectively. $T = \pm 1$ indicates circular polarization, while $T = 0$ and $T = \pm\infty$ indicate linear polarization.

$$\boldsymbol{\kappa} = (\sin\theta, 0, \cos\theta)\,, \qquad \boldsymbol{a} = (0, 1, 0)\,, \qquad \boldsymbol{t} = (\cos\theta, 0, -\sin\theta)\,,$$

$$S = \tfrac{1}{2}(R_+ + R_-)\,, \qquad D = \tfrac{1}{2}(R_+ - R_-)\,,$$

$$R_\pm = 1 - \frac{\omega_{pe}^2}{\omega^2}\frac{\omega}{\omega \mp \Omega_e} - \frac{\omega_{pp}^2}{\omega^2}\frac{\omega}{\omega \pm \Omega_p} - \frac{\omega_{p\mathrm{He}}^2}{\omega^2}\frac{\omega}{\omega \pm \Omega_{\mathrm{He}}}\,,$$

$$P = 1 - \frac{\omega_{pe}^2}{\omega^2} - \frac{\omega_{pp}^2}{\omega^2} - \frac{\omega_{p\mathrm{He}}^2}{\omega^2}\,,$$

$$A = P\cos^2\theta + S\sin^2\theta\,,$$

$$B = (S^2 - D^2)\sin^2\theta + PS(1 + \cos^2\theta)\,,$$

$$C = P(S^2 - D^2)\,,$$

$$F^2 = B^2 - 4AC\,,$$

$$n_\pm^2(\omega, \theta) = \frac{B \pm F}{2A}\,,$$

in the notation defined in § 2.

$K_\pm$ and $T_\pm$ describe the longitudinal and transverse part of the wave polarization, respectively. $T = \pm 1$ corresponds to right (left) circular polarization and $T = 0$ or $T = \pm\infty$ to linear polarization along $\boldsymbol{a}$ and $\boldsymbol{t}$, respectively. In general, the waves are elliptically polarized and $T_\pm$ are orthogonal, i.e., $T_+ T_- = 1$.

Figure 18 illustrates the cold plasma dispersion relation $\omega(k)$ (*left panels*) and the sense of polarization of the waves represented by T (*right panels*), for three different propagation angles of the waves, $\theta = 0°$, 45°, and 90°. Note that for a given frequency ω, there are always two wavenumbers corresponding to the modes denoted with plus and minus signs, but there are three frequencies ("branches") for each wavenumber k (for $\theta \neq 90°$). For $\theta = 0°$ (*top*), the solid branch is left-circularly polarized, since $T = -1$, the dashed branch starts right- and changes to left-circularly polarized at the cutpoint, and the dotted one starts left- and changes to right-circularly polarized.

The polarization properties of the three branches for $\theta = 45°$ are shown in the middle panels. The dashed and dotted branches do not intersect any more, and the waves are now elliptically polarized. The solid branch is linearly polarized for small k values as $T \to -\infty$. With increasing k, the polarization becomes elliptical but still left, and it turns into left circular when $k \to \infty$ as $T \to -1$.

The dashed branch starts linearly polarized at small k, since $T \to 0$. It changes into a right elliptical wave, and it becomes right-circularly polarized as T passes through 1. After that, it is again right elliptical and transforms into a linear wave, as T has a pole at $kc/\Omega_p \sim 115$. At this point, the wave starts to rotate in the opposite direction. As T rises from $-\infty$, the wave is linear, becomes left elliptical, and eventually turns into a circular left wave when $k \to \infty$.

The dotted branch presumably starts left circular for $k = 0$, but it has not been plotted below $kc/\Omega_p = 10$ because of numerical problems in the calculation. Beyond this point, it is left elliptical, then linear as T passes through zero, then right elliptical, and eventually it turns into a right circular wave, as $T \to +1$ for $k \to \infty$.

For $\theta = 90°$, all the waves are linearly polarized and the solid branch has disappeared completely, while the dashed one bends for $kc/\Omega_p > 75$ into a region that we may call helium lower hybrid frequency

REFERENCES

Anders, E., & Grevesse, N. 1989, Geochim. Cosmochim. Acta, 53, 197
Arnaud, M. 1995, private communication
Arnaud, M., & Raymond, J. 1992, ApJ, 398, 394
Arnaud, M., & Rothenflug, R. 1985, A&AS, 60, 425
Breneman, H., & Stone, E. C. 1985, ApJ, 299, L57
Brickhouse, N. S., Raymond, J. C., & Smith, B. W. 1995, ApJS, 97, 551
Brosius, J. W. 1995, private communication
Brosius, J. W., Davila, J. M., Thomas, R. J., & Monsignori-Fossi, B. C. 1996, ApJS, 106, 143
Brosius, J. W., Davila, J. M., Thomas, R. J., & Thompson, W. T. 1994, ApJ, 425, 343
Brosius, J. W., et al. 1993, ApJ, 411, 410
Brosius, J. W., Willson, R. F., Holman, G. D., & Schmelz, J. T. 1992, ApJ, 386, 347
Cane, H. V., McGuire, R. E., & von Rosenvinge, T. T. 1986, ApJ, 301, 448
Cook, J. W., Cheng, C. C., Jacobs, V. L., & Antiochos, S. K. 1989, ApJ, 338, 1176
Cook, J. W., Keenan, F. P., Harra, L. K., & Tayal, S. S. 1994, ApJ, 429, 924
Fisk, L. A. 1978, ApJ, 224, 1048
Garrard, T. L., & Stone, E. C. 1993, Proc. 23rd Int. Cosmic-Ray Conf. (Calgary), 3, 384
Gloeckler, G., Sciambi, R. K., Fan, C. Y., & Hovestadt, D. 1976, ApJ, 209, L93
Grevesse, N., & Noels, A. 1993, in Origin and Evolution of the Elements, ed. N. Prantzos, E. Vangioni-Flam, & M. Cassé (Cambridge: Cambridge Univ. Press), 15
Hara, H., Tsuneta, S., Lemen, J. R., Acton, L. W., & McTiernan, J. M. 1992, PASJ, 44, L135
Hayakawa, S. 1983, ApJ, 266, 370
Ibragimov, I. A., & Kocharov, G. E. 1977, Proc. 15th Int. Cosmic-Ray Conf. (Plovdiv), 11, 340
Jaekel, U., & Schlickeiser, R. 1992, J. Phys. (G), 18, 1089
Klimchuk, J. A., & Gary, D. E. 1995, ApJ, 448, 925
Kocharov, L. G., & Kocharov, G. E. 1984, Space Sci. Rev., 38, 89
Leske, R. A., Cummings, J. R., Mewaldt, R. A., Stone, E. C., & von Rosenvinge, T. T. 1995, ApJ, 452, L149
Luhn, A., et al. 1985, Proc. 19th Int. Cosmic-Ray Conf. (La Jolla), 4, 241
Luhn, A., Klecker, B., Hovestadt, D., & Möbius, E. 1987, ApJ, 317, 951
Mason, G. M., Mazur, J. E., & Hamilton, D. C. 1994, ApJ, 425, 843
Mason, G. M., Mazur, J. E., Looper, M. D., & Mewaldt, R. A. 1995, ApJ, 452, 901
Mason, G. M., Reames, D. V., Klecker, B., Hovestadt, D., & von Rosenvinge, T. T. 1986, ApJ, 303, 849
Ma Sung, L. S., Gloeckler, G., Fan, C. Y., & Hovestadt, D. 1981, ApJ, 245, L45
Melrose, D. B. 1986, Plasma Astrophysics (New York: Gordon & Breach)
Meyer, J. P. 1985a, ApJS, 57, 151
———. 1985b, ApJS, 57, 173
———. 1993a, Adv. Space Res., 13(9), 377
———. 1993b, in Origin and Evolution of the Elements, ed. N. Prantzos, E. Vangioni-Flam, & M. Cassé (Cambridge: Cambridge Univ. Press), 26
———. 1996a, in ASP Conf. Proc. 99, Cosmic Abundances, ed. S. S. Holt & G. Sonneborn (San Francisco: ASP), 127
———. 1996b, in The Sun and Beyond, ed. L. Celnikier & J. Trân Thanh Vân (Gif-sur-Yvette: Editions Frontières), in press
Miller, J. A., & Roberts, D. A. 1995, ApJ, 452, 912

Miller, J. A., & Steinacker, J. 1992, ApJ, 399, 284
Miller, J. A., & Viñas, A. F. 1993, ApJ, 412, 386 (MV)
Miller, J. A., Viñas, A. F., & Reames, D. V. 1993a, Proc. 23rd Int. Cosmic-Ray Conf. (Calgary), 3, 13 (MVRa)
———. 1993b, Proc. 23rd Int. Cosmic-Ray Conf. (Calgary), 3, 17 (MVRb)
Murphy, R. J., Ramaty, R., Kozlovsky, B., & Reames, D. V. 1991, ApJ, 371, 793
Nitta, N., et al. 1991, ApJ, 374, 374
Ogilvie, K. W., Geiss, J., Gloeckler, G., Berdichevsky, D., & Wilken, B. 1993, J. Geophys. Res., 98, 3605
Ohsawa, Y. 1993, J. Phys. Soc. Japan, 62, 2382
Pallavicini, R., Serio, S., & Vaiana, G. S. 1977, ApJ, 216, 108
Press, W., Flannery, B. P., Teukolky, S. A., & Vetterling, W. T. 1990, Numerical Recipes (New York: Cambridge Univ. Press)
Pye, J. P., Evans, K. D., Hutcheon, R. J., Gerassimenko, M., Davis, J. M., Krieger, A. S., & Vesecky, J. F. 1978, A&A, 65, 123
Ramaty, R., Mandzhavidze, N., Kozlovsky, B., & Murphy, R. J. 1995, ApJ, 455, L193
Reames, D. V. 1990, ApJS, 73, 235
———. 1993, Proc. 23rd Int. Cosmic-Ray Conf. (Calgary), 3, 388
———. 1995, Adv. Space Res., 15 (7), 41
Reames, D. V., Meyer, J. P., & von Rosenvinge, T. T. 1994, ApJS, 90, 649 (RMvR)
Riyopoulos, S. 1991, ApJ, 381, 578
Saba, J. L. R. 1995, private communication
Saba, J. L. R., & Strong, K. 1991a, ApJ, 375, 789
Saba, J. L. R., & Strong, K. 1991b, Adv. Space Res., 11 (1), 117
Schlickeiser, R. 1995, A&A, 294, 695
Schlickeiser, R., & Steinacker, J. 1989, Sol. Phys., 122, 29
Schmelz, J. T. 1995, Adv. Space Res., 15 (7), 77
Schmelz, J. T., Holan, G. D., Brosius, J. W., & Gonzalez, R. D. 1992, ApJ, 399, 733
Schmelz, J. T., Holman, G. D., Brosius, J. W., & Willson, R. F. 1994, ApJ, 434, 786
Scudder, J. D. 1992, ApJ, 398, 319
Sheeley, N. R. 1995, private communication
Steinacker, J., & Miller, J. A. 1992, ApJ, 393, 764 (SM)
Swanson, D. G. 1989, Plasma Waves (New York: Academic)
Temerin, M., & Roth, I. 1992, ApJ, 391, L105
Tu, C.-Y., Marsch, E., & Thieme, K. M. 1989, J. Geophys. Res., 94, 11739
Tylka, A. J., Boberg, P. R., Adams, J. H., Beahm, L. P., Dietrich, W. F., & Kleis, T. 1995, ApJ, 444, L109
Varvoglis, H., & Papadopoulos, K. 1983, ApJ, 270, L95
Waljeski, K., Moses, D., Dere, K. P., Saba, J. L. R., Strong, K. T., Webb, D. F., & Zarro, D. M. 1994, ApJ, 429, 909
Wang, Y. M. 1994, ApJ, 437, L67
Wang, Y. M., Sheeley, N. R., & Nash, A. G. 1990, Nature, 347, 439
Weatherall, J. 1984, ApJ, 281, 468
Winglee, R. M. 1989, ApJ, 343, 511
Yoshida, T., & Tsuneta, S. 1996, ApJ, 459, 342
Zhang, T. X. 1995, ApJ, 449, 916
Zhou, Y., & Matthaeus, W. H. 1990, J. Geophys. Res., 95, 10291